Engineering Failure Analysis 144 (2023) 106943

Contents lists available at ScienceDirect

Engineering Failure Analysis

journal homepage: www.elsevier.com/locate/engfailanal

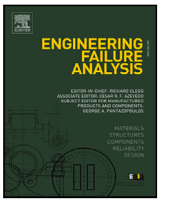

Thin steel plates exposed to combined ballistic impact and partially confined airblast loading

Benjamin Stavnar Elveli [a,b,*], Ole Vestrum [c], Knut Ove Hauge [c], Torodd Berstad [a,b], Tore Børvik [a,b], Vegard Aune [a,b]

[a] Structural Impact Laboratory (SIMLab), Department of Structural Engineering, NTNU – Norwegian University of Science and Technology, NO-7491 Trondheim, Norway
[b] Centre for Advanced Structural Analysis (CASA), NTNU, NO-7491 Trondheim, Norway
[c] Research and Development Department, Norwegian Defence Estates Agency, 0103 Oslo, Norway

ARTICLE INFO

Keywords:
Ballistic impact
Blast loading
Particle blast method
ALE
LS-DYNA

ABSTRACT

Pre-formed defects created by high-velocity impact have the potential to reduce the structural integrity of lightweight, flexible structures. This study evaluates the effect of complex, partially confined detonations on thin steel plates with realistic pre-formed defects. Target plates containing pre-cut circular holes with a diameter of 8.0 mm are compared to target plates exposed to an initial ballistic impact from 7.62 mm APM2 projectiles. The target plates were exposed to blast loading generated from detonating C-4 inside a steel tube. The stand-off distance was fixed and set equal to the tube radius, where the rear end of the tube was kept open. All blast tests were recorded with several pressure sensors, synchronized with two high-speed cameras monitoring the dynamic response of the target plates. This allowed for a reliable experimental procedure, serving as a benchmark for different numerical methods. For similar loading conditions, the target plates containing initial ballistic impact showed a reduced fracture resistance during blast loading compared to the target plates with pre-cut circular holes. Two different numerical approaches were tested and compared, i.e., a purely Lagrangian particle-based approach and a fully coupled simulation approach using an ALE description of the blast domain. The ALE simulations were found to underestimate the structural response, while the particle-based approach overestimated the structural response.

1. Introduction

Blast waves can occur in various environments and typically originates form accidental, industrial or intended explosions [1–3]. Hazardous fragments are often accelerated by and move together with the blast wave. Such objects may be parts originating from an explosive's container or debris from surrounding structures, i.e., primary and secondary fragments. Several studies indicate that the combined effects of blast and fragment impact can be more severe than the blast loading acting alone (see e.g., [4–8]). Considering a cased explosive, the initial fragment velocity is normally much smaller than the initial velocity of the blast wave. As the blast wave expands, its velocity is reduced at a higher rate than the fragments. This means that the high velocity fragments may strike before, during, or after the arrival of the blast wave, depending on the distance [8].

* Corresponding author at: Structural Impact Laboratory (SIMLab), Department of Structural Engineering, NTNU – Norwegian University of Science and Technology, NO-7491 Trondheim, Norway.
E-mail address: benjamin.s.elveli@ntnu.no (B.S. Elveli).

https://doi.org/10.1016/j.engfailanal.2022.106943
Received 27 September 2022; Received in revised form 13 November 2022; Accepted 14 November 2022
Available online 17 November 2022

Several studies exists on blast-loaded plates with pre-cut idealized defects, which represents fragment impact prior to blast loading [9–15]. The pre-cut defects significantly reduce the blast resistance of the target plates. That is, fracture tends to occur around the defects rather than at the supports, which is a common fracture mode for target plates without any pre-cut defects [16–18]. Granum et al. [12] found that the shape, orientation and number of pre-cut defects affected both the fracture resistance and the crack path in the target plates. Elveli et al. [19] further investigated the effect of pre-formed ballistic impact holes compared to pre-cut circular holes for thin steel plates exposed to blast-like loading conditions in a shock tube facility. As expected, the target plates with pre-formed ballistic impact holes showed a reduced fracture resistance compared to the plates with pre-cut circular holes. All crack propagations were initiated from the petalling cracks around the ballistic impact hole. The pre-formed ballistic impact holes and pre-cut circular holes were located at the plate center, and the loading characteristics showed similarities to that of a far-field detonation. That is, a uniformly distributed pressure field with a relatively low peak pressure and a large duration of the positive phase. A novel experimental technique was recently suggested by Atoui et al. [20], where a solid explosive with an embedded steel sphere was detonated at the entrance of an explosive-driven shock tube. The objective of the study was to control the time interval between the arrival of the steel sphere and the shock wave at the target. The experimental setup succeeded in creating repeatable loading conditions, where the spatiotemporal evolution of both the shock and the sphere were recorded using optical diagnostics.

Compared to blast loads generated in a shock tube or by detonations in free air, the number of studies on confined explosions are more limited. Confined blast loads are also more complex than those in free air. Previous studies [21,22] have shown that the common design manual UFC-3-340-02 [23] is unable to predict a satisfactory loading history and pressure distribution from confined detonations. Because of the interactions between the propagating shock and the confinement, the loading history typically consists of several pressure peaks [21,24,25] with amplified magnitudes [26–28], and hence, significantly increased damage potentials [29]. The multiple pressure peaks tend to decrease towards a static overpressure, or back to atmospheric conditions depending on the venting of the confinement. Although each pressure peak evaluated alone may represent a relatively short duration, the duration of the full loading event is typically much longer than what is found for free air detonations.

However, the pressure history, pressure distribution and deformation mode are all significantly affected by the degree of confinement and the position of the explosive charge. For circular mild steel plates exposed to confined blast loading, changes in stand-off distance affect the global deformation response. At stand-off distances smaller than the confinement radius, the plates deform as a global dome with a superimposed local dome around the plate center. As the stand-off is set to a larger distance than the distance to the confinement, the plates deform in a global dome (see e.g., [30]).

A similar study was performed by Yuan et al. [31], where the dynamic response of thin square steel plates were investigated for several stand-off distances for fully confined detonations. By placing one deformable steel plate in each end of a squared confinement tank, two different stand-off distances were studied for each detonation. The plate with the largest stand-off distance consistently experienced the largest maximum displacements, through a global dome deformation mode. The closest stand-off distance resulted in smaller deformations, but with a superimposed local dome on the global dome, similarly as the observations in Ref. [30]. The larger stand-off led to lower peak pressures and longer durations for the transferred impulse. The total impulse was the largest for the closest plate, but the saturated impulse was seemingly larger for the plate with the largest stand-off. Generally, for confined detonations, it is observed that if the explosive charge is positioned at a distance larger than the distance to the confinement, the incoming pressure takes a more uniform distribution. For stand-off distances smaller than the distance to the confinement, the pressure distribution of the initial pressure peak takes a distribution similar to that observed for unconfined detonations.

Zhang et al. [15] studied thin square steel plates with different pre-cut defects exposed to fully confined blast loads. The response of the plates without any defects were compared to the plates containing circular and square holes. It was found that the target plates with pre-cut holes experienced smaller deformations than the plates without any defects. This was explained by the venting effect of the holes and is contrary to previous findings in studies on similar plate geometries exposed to blast loads from a shock tube facility (see e.g., [11,32]). It is also noted that only the target plates with square holes experienced fracture during blast loading. Hence, the circular holes showed a larger resistance to fracture.

As confined blast loading is dependent upon interactions with the confinement on its way towards the blast-loaded structure, simple pressure time histories from free-field detonations (e.g., ConWep) are seldom an option. To capture the pressure build-up during the propagation phase, it is required with a fully coupled fluid–structure interaction (FSI) approach including the explosive detonation, blast wave propagation and the structural response in the same simulation. A common choice is the Arbitrary Lagrangian–Eulerian (ALE) description. Here, the structural domain follows the traditional Lagrangian description and solved using the explicit finite element method (FEM). The fluid domain is also described using FEM, but through a framework which is neither Eulerian nor Lagrangian [33–38]. The ALE description of multi-material models describing the detonation of high explosives follows the so-called operator split method, where the calculations within each time step is divided into two phases [39]. First, the mesh moves with the fluid materials according to a Lagrangian description. In the following phase, the distorted mesh is remapped back to its original configuration through an advection step. The fluid–structure coupling is described through a penalty-based contact formulation on the penetration of the fluid into the structural domain.

This approach was successfully applied in Refs. [15,31,40–42]. The ALE approach with fully coupled FSI simulations is often computationally expensive, and the description of the blast loading tend to be slightly underestimated. In Ref. [15], the target plate displacement was underestimated with approximately 10%, whereas Ref. [31] found that the agreement between numerical and experimental observations varied with the stand-off distance. As a too coarse discretization of the fluid domain smears out the shock discontinuity, and gives too low pressure peaks, convergence studies should be performed. Another issue with the ALE approach is related to the fluid–structure coupling, where material leakage is commonly encountered. Langdon et al. [41] suggested that

the discretization of the structure must be significantly finer than the discretization of the fluid domain to overcome this issue. An element size ratio of 1/4 between the structural and fluid domains resulted in no leakage. A simpler and computationally more efficient approach is formulated through the particle blast method (PBM). This blast modeling approach is based on the corpuscular method used for airbag deployment in LS-DYNA [43]. Later it was modified and successfully validated to also represent blast loads by Børvik et al. [44,45].

The literature review demonstrates that the combined effect of fragment impact and confined airblast loading is still an open research topic. Thus, there is a need for more detailed experimental studies and to evaluate the performance of current computational methods in such load environments. These studies are relevant in designing protective structures against accidental, industrial or intended explosions in enclosed spaces. This motivated studies on target plates exposed to blast loading generated from detonating C-4 in a vented tube, resulting in more complex loading conditions than that in previous studies on combined ballistic impact and blast loading (see e.g. Ref. [19]). In turn, this allowed for the evaluation of more advanced numerical techniques to describe partially confined airblast loading events. The stand-off distance was fixed and set equal to the tube radius, where the rear end of the tube was kept open. This was done in an attempt to reduce the sequential loading that is expected from a fully confined detonation. The target plates were thin steel plates with pre-formed defects of either pre-cut circular holes with a diameter of 8.0 mm or ballistic impact holes from 7.62 mm APM2 projectiles.

The main objectives of this study are: (1) establish a repeatable and controlled experimental setup to study the dynamic response of structures subjected to loading caused by partially confined detonations; (2) investigate the effect of a more complex blast environment on the response of thin steel plates with pre-formed defects resembling those from fragment impact; (3) to validate and compare different numerical approaches for the modeling of the partially confined blast environment against experimental observations.

2. Experimental study

In this study, the dynamic response of thin steel plates exposed to partially confined airblast loading has been investigated. Full plates, plates containing pre-cut circular holes, and plates with pre-formed ballistic impact holes were evaluated. All blast tests were performed at an indoor testing facility operated by the Norwegian Defence Estate Agency (NDEA). The experimental setup and all corresponding measuring equipment are described in Section 2.1, while the results are given in Section 3.

2.1. Experimental setup

All blast tests were carried out by detonating an explosive charge of Composition C-4 inside a steel tube with a length of 1 m and an inner diameter of 0.4 m, as illustrated in Fig. 2(a). The C-4 charges were suspended vertically from the highest point of the tube's hull at a horizontal distance of 0.2 m from the target plates and as close to the center as possible in the radial direction. As the position of the explosives was kept fixed in all tests, two different charge masses of 10 g and 20 g were used to vary the blast intensity. Due to safety-related constraints at the indoor testing facility, it was decided to limit the charge mass to 20 g of C-4 for the partially confined detonations. The target plates were clamped to the flange of the tube at the right end in Fig. 2(a). The inner diameter of the clamping frame was equal to the inner diameter of the tube. A more detailed illustration of the clamping frame is given in Fig. 2(b). For fully confined detonations, the loading history on the target plates would consist of several pressure peaks as the shock travels back and forth inside the tube [21,24,25]. In turn, this would also increase the duration of the total loading history. To obtain a controlled loading on the target plates with a shorter duration, it was decided to keep the rear end open in all blast tests [46]. The full assembly with the steel pipe, target plate and clamping frame were put on a stack of wooden pallets, and strapped to the floor as shown in Fig. 1.

To study the effect of pre-formed defects in thin steel plates exposed to the partially confined airblast loading, three different plate configurations were studied. One configuration without any pre-formed defects, denoted FP, one configuration containing pre-cut circular holes, denoted C, and one configuration containing an initial ballistic impact hole, denoted B. All target plates had a thickness of 0.8 mm and the geometries of the plates are illustrated in Fig. 2(b–d). The two hole geometries are adopted from Ref. [19].

The blast response of the steel plates were recorded with two synchronized Phantom v2012 high-speed cameras with a sampling rate of 22 626 frames per second at a resolution of 1200 x 800 pixels. The two cameras were positioned in a stereoscopic setup as shown in Fig. 3. Prior to each test, the target plates were spray painted with a black and white speckle pattern. This enables measurements of the displacement fields of the target plates during blast loading by using the in-house three-dimensional digital image correlation (3D-DIC) software eCorr [47]. The movement of the testing rig was also tracked in eCorr by applying checkerboard stickers to the clamping frame around the target plates.

All pressure histories were measured using Kistler 603B pressure sensors with a sampling rate of 500 kHz and a pressure range of 200 bar [48]. The pressure sensors were placed at four different locations as shown in Figs. 3 and 4. The location of the pressure sensors P11 and PR02, are indicated in Fig. 3. Pressure sensor P11 was mounted on the inner tube wall, 600 mm away from the explosive charge. PR02 was placed on a fixed table outside the open end of the tube, with a height aligned with the center of the tube. A breakwire was placed inside each explosive charge, which recorded the current in the wire at the same sampling rate as the pressure sensors. The time of the detonation is established as the wire is cut by the detonation of the charge. All pressure and deformation histories are plotted with the time of detonation defined as t=0 ms.

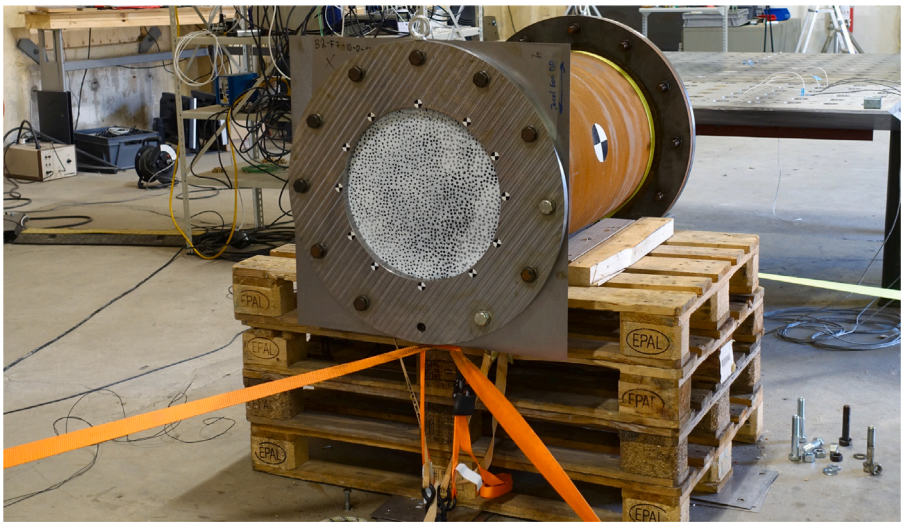

Fig. 1. The testing rig used for partially confined detonations with a mounted target plate prepared for blast testing.

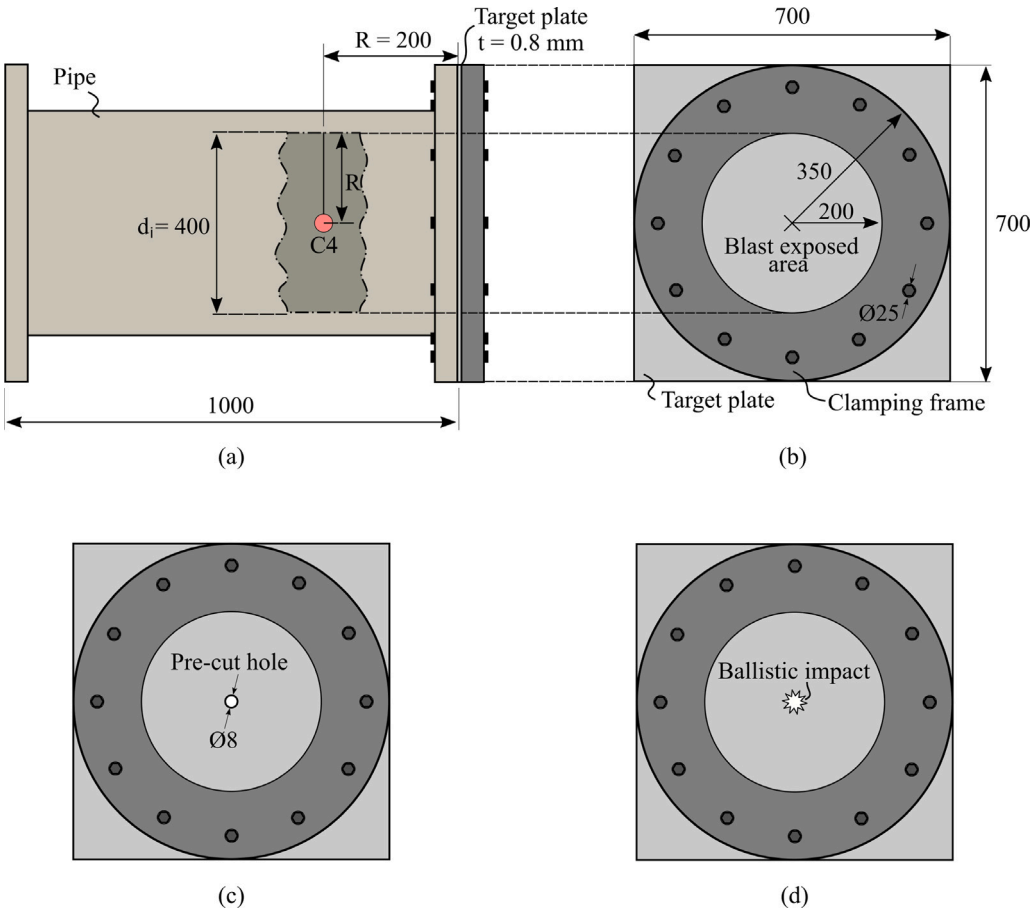

Fig. 2. Schematic of the experimental setup: (a) The dimensions of the test rig and the position of the explosive charge, (b) the dimensions of the clamping frame and target plates, and the plate geometries containing (c) pre-cut circular holes and (d) pre-formed ballistic holes. All dimensions are in mm.

As an attempt to estimate the pressure on the blast-exposed surface of the deformable plates, additional blast tests using a 199 kg pendulum were performed. The schematic presentation of the pendulum is shown in Fig. 4. Two pressure sensors were mounted

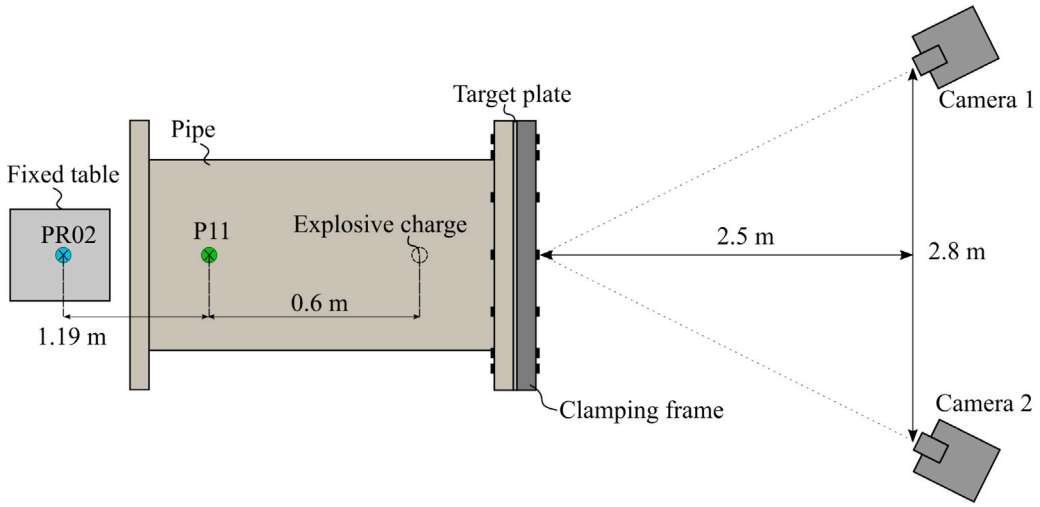

Fig. 3. The setup for high-speed camera recordings and the positioning of the pressure sensors for all experiments on thin steel plates.

Table 1
Experimental program.

Charge mass	FP	C	B	P
10 g	FP_10_1	C_10_1	B_10_1	P_10_1
	–	C_10_2	B_10_2	P_10_2
	–	C_10_3	B_10_3	–
20 g	FP_20_1	C_20_1	B_20_1	P_20_1
	–	C_20_2	B_20_2	P_20_2
	–	C_20_3	B_20_3	–

on the blast-exposed surface of the pendulum, denoted P01 and P02 with positions given in Fig. 4(a). As the confinement tube is fixed and exposed to extreme loads, significant structural vibrations are expected. These vibrations tend to affect the measurements from the pressure sensors. The pendulum was attached to the ceiling, 4 m above the testing rig using four steel wires, as shown in Fig. 4(b)–(c). The pendulum was not attached to the pipe, but rested against the pipe flange. This means that the pendulum is free to move after the detonation and that movement is restricted only by the wires. It is assumed that this leads to less high-frequency oscillations in the pendulum, resulting in cleaner pressure measurements. The total blast-exposed area of the pendulum has a diameter of 700 mm, identical to the outer diameter of the flanges of the tube. As the pendulum rests at the end of the tube before detonation, the initial blast-exposed area coincides with the inner diameter, d_i=400 mm, of the tube. The sensors P01 and P02 are located within the initial blast-exposed area.

The three plate geometries and the pendulum were all tested against the two different charge masses of 10 g and 20 g of C-4. For the target plates containing pre-cut circular holes (C) and the target plates exposed to initial ballistic impact (B), three repetitions were performed for each unique configuration. Two repetitions were also conducted for the pendulum tests. Lastly, for the full plate geometry (FP) only one test was performed. This gives a total of 18 partially confined airblast experiments. The corresponding test matrix is given in Table 1, where each test is labeled according to the naming convention XX_YY_ZZ. Here, XX denotes the geometry of the test sample, i.e., FP for the full plate, C for the pre-cut circular hole, B for the initial ballistic impact hole, or P for the pendulum. YY refers to the two different charge masses in grams, i.e., 10 or 20. Lastly, ZZ denotes the repetition number of the same configuration.

2.2. Target plate material

All target plates applied in this study were manufactured from a medium-strength and high-hardening dual phase steel called Docol 600DP. The steel plates were cold rolled to the desired thickness of 0.8 mm and produced by Swedish Steel Ltd. (SSAB). During the production process, the plates are heat treated after cold rolling to obtain the desired properties of the material and microstructure [49]. The manufacturer reported a yield strength in the range 350–450 MPa and an ultimate tensile strength in the range 600–700 MPa. Docol 600DP is a material developed mainly for the automotive industry due to its good formability.

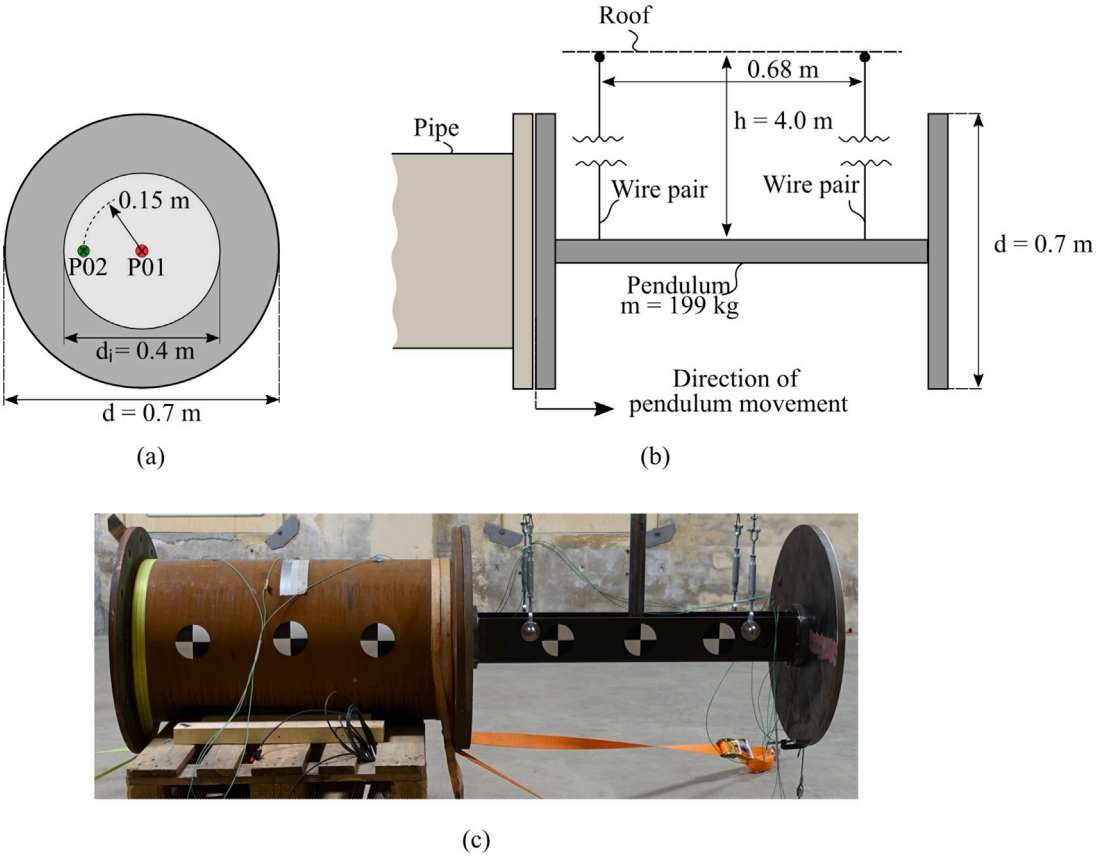

Fig. 4. Schematic illustration of the ballistic pendulum tests: (a) The blast exposed area of the pendulum with indicated locations for the two pressure sensors, P01 and P02, and (b) the dimensions of the pendulum assembly. In (b) it is noted that each wire pair represents two wires with an out-of-plane distance of 100 mm. A photograph of the pendulum and confinement pipe is given in (c). Note that pendulum is not attached to the pipe, but rests against the pipe flange.

Quasi-static tension tests of the plate material were performed using an Instron 5566 universal testing machine to document the mechanical properties of the steel material. The tension test specimens were cut in three different directions, 0°, 45°, and 90° relative to the rolling direction of the target plates. Three repetitions were performed in each direction. The dimensions of the tensile test specimen are given in Fig. 5(a). With a gauge length of 70 mm, the applied deformation rate 2.1 mm/min corresponds to an initial strain rate of $\dot{\varepsilon}_0 = 5 \cdot 10^{-4}$ s^{-1}.

The force F was measured by the load cell of the testing machine and the elongation ΔL was obtained from 2D-DIC using a virtual extensometer with an initial length of L_0=60 mm. The force measurements were synchronized with images sampled at a rate of 4 Hz. The engineering stress and strain was then calculated by Eq. (1), where A_0 denotes the measured gauge area of each test specimen.

$$s = \frac{F}{A_0} \qquad \varepsilon = \frac{\Delta L}{L_0} \tag{1}$$

The engineering stress–strain curves in Fig. 5 confirm the yield and ultimate tensile stress reported by the manufacturer. However, there are minor deviations in engineering stress between the three directions. The 90° experienced higher engineering stress and a smaller elongation to fracture than the 0° and 45° tests. Similar trends were found for the uniaxial tension tests in Refs. [11,50] for the comparable material Docol 600DL, also produced by SSAB. Here, in both cases, it was concluded that the plastic anisotropy was negligible.

2.3. Ballistic impact tests

The ballistic impact holes were created by firing a 7.62 mm APM2 projectile from a smooth-bore Mauser rifle mounted in a firing-rig with an initial velocity of around 900 m/s. One single shot was fired against the center of the target plates, perpendicular to the surface of the sheet. The procedure for the ballistic testing was done under identical conditions as in Elveli et al. [19] and is therefore only briefly described herein. The intention of the ballistic impact event was to introduce a more realistic fracture mode

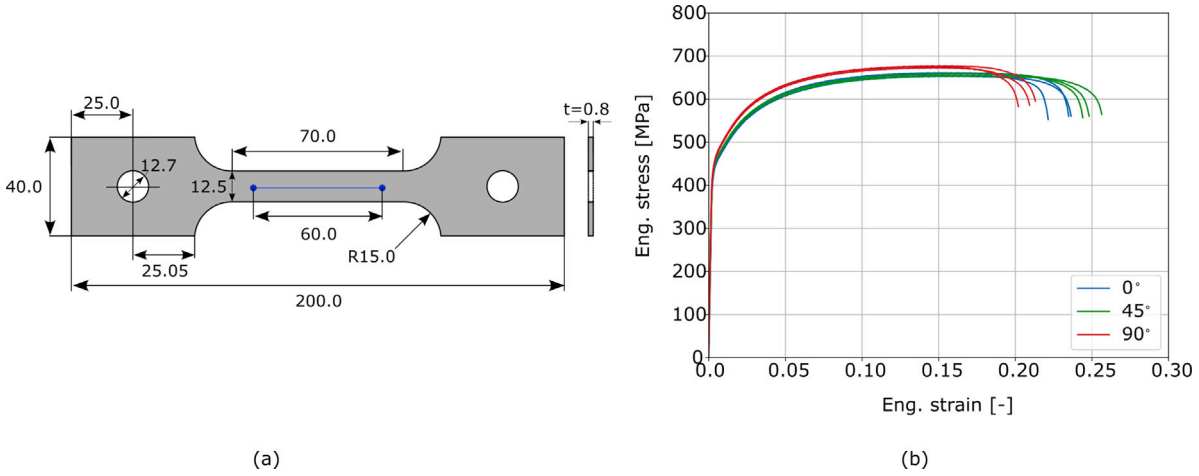

Fig. 5. Uniaxial tension tests: (a) Sketch of the dog-bone specimen and the position of the virtual extensometer marked with a blue line, and (b) the corresponding engineering stress–strain curves for the Docol 600DP material. All dimensions are in mm. (For interpretation of the references to colour in this figure legend, the reader is referred to the web version of this article.)

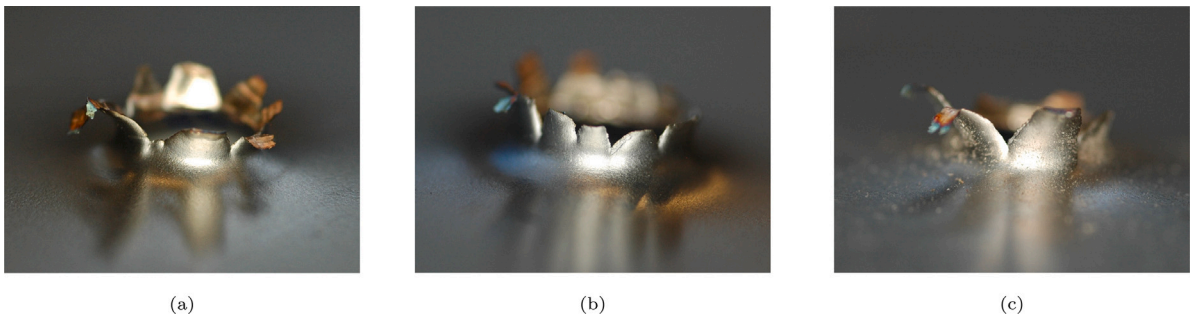

Fig. 6. Three representative images of the obtained petalling fracture mode from the ballistic impact tests.

to the target plates prior to the blast load. For a better comparability to the target plates containing 8.0 mm pre-cut circular holes, it was desired to produce bullet holes with as little global deformation as possible.

The initial projectile velocity of 900 m/s was significantly higher than the ballistic limit velocity of the 0.8 mm target plates. The resulting velocity reduction after impact with the target plates was in the range of 1%–2%. Further, all target plates failed by petalling and experienced only local plastic deformations and fracture around the impact hole. Three representative images of the obtained fracture mode from the ballistic impact event are given in Fig. 6. It should be noted that an evaluation of the ballistic capacity of the target plates was not performed, as it was considered beyond the scope of this study.

3. Partially confined detonations

The results of all airblast experiments are presented in this section and are divided into three main parts. First, the measured pressure histories are presented with the main objective of understanding the characteristics of the loading history and its repeatability between tests. Secondly, the global deformations of the target plates are considered through deformation histories obtained by 3D-DIC analyses of the high-speed camera recordings. Lastly, the fracture resistance of the different plate geometries are evaluated.

3.1. Pressure measurements

To date, there are no experimental techniques capable of measuring full-field surface pressures acting on thin plates undergoing large deformations [51]. This motivated the blast tests on the 199 kg pendulum exposed to identical loading conditions. As shown in Fig. 4(a), the reflected pressure was measured at two locations (P01 and P02) on the blast-exposed surface of the pendulum. The corresponding pressure histories are compared for the two repetitions in Fig. 4(a) and (b), for the 10 g and 20 g detonations, respectively. All pressure histories have been adjusted according to the breakwire, so that the detonation occurs at t=0 ms.

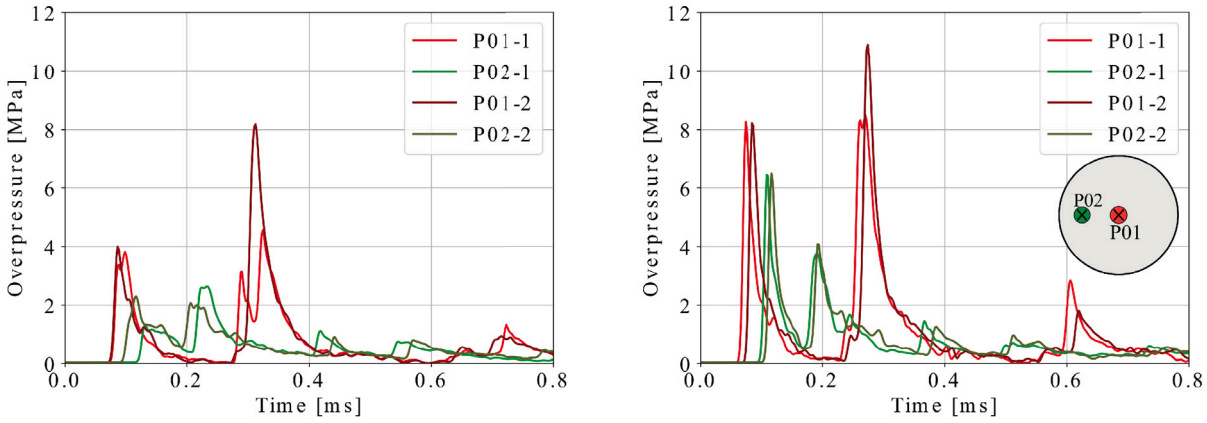

(a) 10 g C-4 (b) 20 g C-4

Fig. 7. The reflected pressure histories on the blast-exposed surface of the pendulum, measured at sensors P01 and P02 (see Fig. 4). The recorded pressure is compared for both of the two repetitions of the 10 g detonation in (a) and the 20 g detonation in (b). The position of the two sensors is also indicated in (b).

As the explosive charge was placed one tube radius away from the pendulum, the first pressure peak represents the incoming shock impacting the pendulum without any interaction with the tube wall. As P01 has the shortest distance to the explosive charge, the first pressure peak arrives at P01 before P02. The second pressure peak occur as the shock is reflected at the tube wall, and then redirected towards the center of the pendulum. P02 is positioned closer to the tube wall, and therefore, the delay between the first and second peak is much shorter for P02 than for P01. It is also observed that the secondary pressure peak at P02 is significantly smaller than the first. For P01, the secondary pressure peak is similar, or even slightly larger than the first reflection. This could be explained by the axisymmetry in the confinement tube. As the pressure reflects at the tube wall, all reflections will eventually meet at the tube center and amplify the secondary pressure peak measured at P01.

Between the repeated tests the magnitude of the pressure peaks, the duration, and the overall behavior were comparable within each of the two charge masses. However, small deviations were observed in the time of arrival between the two 20 g charge tests (see Fig. 7(b)). Both P01-2 and P02-2 experienced an identical offset relative to P01-1 and P02-1. All measurements were time-shifted similarly by the breakwire, and the reason for the slight offset is unknown. Another difference between the two repetitions, observed for both charge masses, is the magnitude of the second pressure peak for sensor P01. P01-2 experienced a larger magnitude of the second pressure peak than P01-1. It is unclear whether this is caused by actual differences in the loading history, or if it is caused by disturbances of the sensor.

From the measurements of P01 and P02 in Fig. 7 it is evident that the loading history on the blast-exposed surface of the pendulum is non-uniform and has a relatively short duration for both charge masses. The majority of the loading history experienced a duration of around 0.35 ms, with only minor pressure peaks from this point and out. Between the two different charge masses, the initial pressure peak at P01 is halved from 8 MPa for the 20 g charge, to 4 MPa for the 10 g charge. It should be noted that the measured peak pressures are limited by the sampling rate of the pressure sensors, and that higher pressures could occur between measurements.

For the deformable steel plates, the only available pressure measurements are from sensor P11 and PR02. As illustrated in Fig. 3, P11 was mounted along the inner wall of the tube, while PR02 was positioned on a fixed table right outside the free end of the tube. The corresponding pressure measurements from pressure sensors P11 and PR02 are presented in Fig. 8 for all 10 g detonations on deformable steel plates with and without pre-cut defects.

The pressure histories obtained from both P11 and PR02 are more noisy than those measured for P01 and P02 in Fig. 7. For the measurements at P11, large variations in both the initial peak pressure and the overall pressure history was found. Some of the measurements even experienced oscillations before the arrival of the shock wave, as seen in Fig. 8(a). A more clean rise in pressure up to the initial peak was found for the measurements from PR02, as seen in Fig. 8(b). Also here, some oscillations were observed after the initial pressure peak. These oscillations or noise in the pressure measurements for P11 and PR02 are assumed to be caused by vibrations in the structures that are instrumented with the pressure sensors. However, if we consider the measurements from PR02 and further only the initial pressure peak, the loading history seems to be quite consistent across all tests within a similar charge mass. As the 20 g detonation showed similar trends for P11 and PR02, the pressure histories are not plotted. All measured peak pressures at P11 and PG02 are listed in Table 2.

To summarize, it was challenging to obtain clean pressure measurements for all blast tests, especially for tests on thin, deformable steel plates where the sensors had to be mounted to the test rig. The reflected pressure measurements from the blast-exposed surface of the pendulum showed clean pressure peaks, with minor fluctuations, and good repeatability of the loading histories. The repeatability of the loading history seems to be quite consistent also for the deformable steel plates, if the measurements from PR02 are considered.

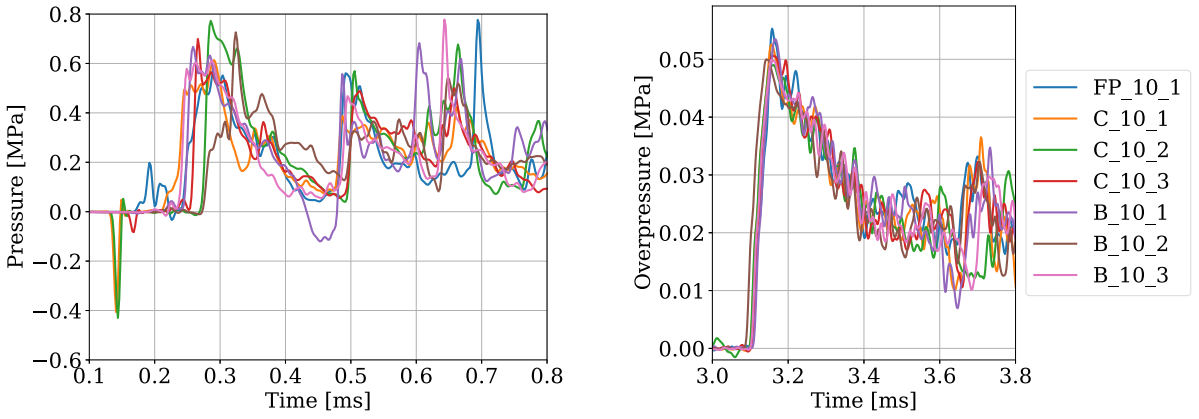

(a) P11 (b) PR02

Fig. 8. Pressure measurements from the 10 g detonations for pressure sensors P11 and PR02 with positions indicated in Fig. 3. The applied sensor corresponding to each plot is given in the sub-caption.

3.2. Deformation response

To obtain reliable displacement fields from the 3D-DIC analysis, the spray-painted speckle pattern must remain intact throughout the dynamic response of the target plates. Unfortunately, the spray paint was detached from the thin steel plates around the plate center for some of the tests. Another 3D-DIC issue occurred for the target plates containing pre-formed holes, as the fireball from the detonation saturated the high-speed camera recordings for some of the images during the deformation process. That is, the visibility of the recorded images was poor due to the strong light resulting from the detonation process. This issue was overcome by simply skipping the images with poor quality from the DIC analysis. Figs. 9 and 10 show representative deformation profiles from the successful 3D-DIC analyses. The deformation profiles correspond to the out-of-plane displacements at a given time along a vector starting at the plate boundary and moving through the plate center.

Fig. 9 shows the deformation profiles for tests FP_10_1 and FP_20_1 for all recorded deformation states from zero displacement and up to the maximum displacement. The total time-span from the detonation up to maximum deformation is given in the upper right corner of each plot. For each plot, four main states of deformation are labeled according to factors relative to the maximum displacement, i.e., factors of 0.25, 0.50, 0.75 and 1.0. The green dotted lines indicate the plate movement in-between the labeled states of deformation. It should be noted that the spray paint detached around the center of the FP_10_1 test right before maximum displacement was reached, and therefore the center portion of the “1.0” deformation profile was not obtained.

It is observed that the deformation process is characterized by three main phases (see Fig. 9). During the first phase, the blast-exposed area of the target plate is activated and moves as a rigid body. A plastic hinge starts to propagate from the outer boundary of the target plate towards the center. Between the plastic hinge and the boundary, the plate takes a triangular shape, with limited visual curvature. This takes place mainly up to the 0.5 deformation profile, marked with blue in Fig. 9(c).

In the second phase, the plastic hinges gradually started to move faster than the center portion of the plate in the out-of-plane direction. From the mid-point displacement plot in Fig. 9(d), the deformation rate is decreasing slightly between the orange and the blue dots. Between the blue and purple deformation profiles in Fig. 9(c), a local dent starts to form around the center, as the mid-point moves too slow to keep up with the rest of the plate. This continues until approximately 0.75 ms after the detonation.

In the third and last phase, the local dent at the center of the plate rapidly starts to accelerate outwards. At this point, the plastic hinges has moved almost all the way to the plate center, and the deformation profile takes a triangular shape. With respect to the mid-point, this is also the phase with the largest deformation rate, seen as a rapid increase of displacements in Fig. 9(d). The deformation profile at maximum displacement takes the shape of a global dome with a superimposed local dome around the plate center, similar to the findings in Refs. [18,30].

The entire deformation process up to the time of maximum deformation takes about 1 ms from the time of detonation. Compared to the loading rate presented in Fig. 7, it is observed that the entire loading history ends after about 0.4 ms. According to the pressure measurements, the movements from the blue deformation profile in 9(c) and up to maximum deformation occur without any applied loading from the detonation. After the maximum displacement of about 50 mm for the FP_20_1 plate was reached, minor elastic oscillations between 48.7 mm and 47.1 mm occurred.

As expected, the reduction in the charge mass from 20 g in test FP_20_1 to 10 g in test FP_10_1 reduced both the maximum deformations and the deformation rates. This is seen by comparing the deformation histories from the 20 g detonation in Fig. 9(c) and (d), to the 10 g detonations in Fig. 9(a) and (b). Even though the deformations and deformation rate are observed to decrease in test FP_10_1, the main trends in the deformation response are similar, but less pronounced. Before studying the fracture resistance of the target plates with pre-formed defects, the global response was evaluated briefly. Fig. 10 compares the deformation profiles for

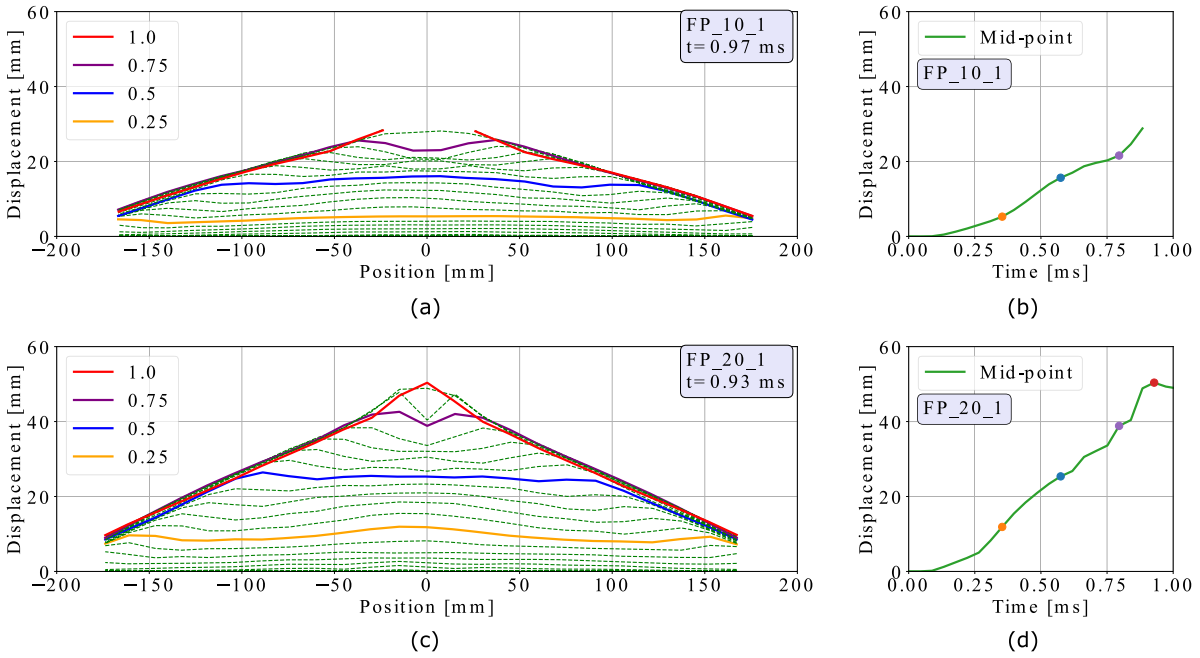

Fig. 9. Deformation profiles for tests FP_10_1 in (a) and FP_20_1 in (c). For each plot, four main states of deformation are labeled relative to the maximum displacement, i.e., factors of 0.25, 0.50, 0.75 and 1.0. The green dotted lines indicate the plate movement in-between the labeled states of deformation, with a time difference of $\Delta t = 0.044$ ms between each sampling. The total time between the detonation and the occurrence of the maximum displacement t is given in the upper left corner of each plot. The corresponding mid-point displacements versus time are plotted for both tests in (b) and (d). It is noted that the spray paint detached around the plate center for the FP_10_1 test, and hence, the center portion of the deformation profile as well as the last part of the mid-point displacement response was excluded from the plots in (a) and (b). (For interpretation of the references to colour in this figure legend, the reader is referred to the web version of this article.)

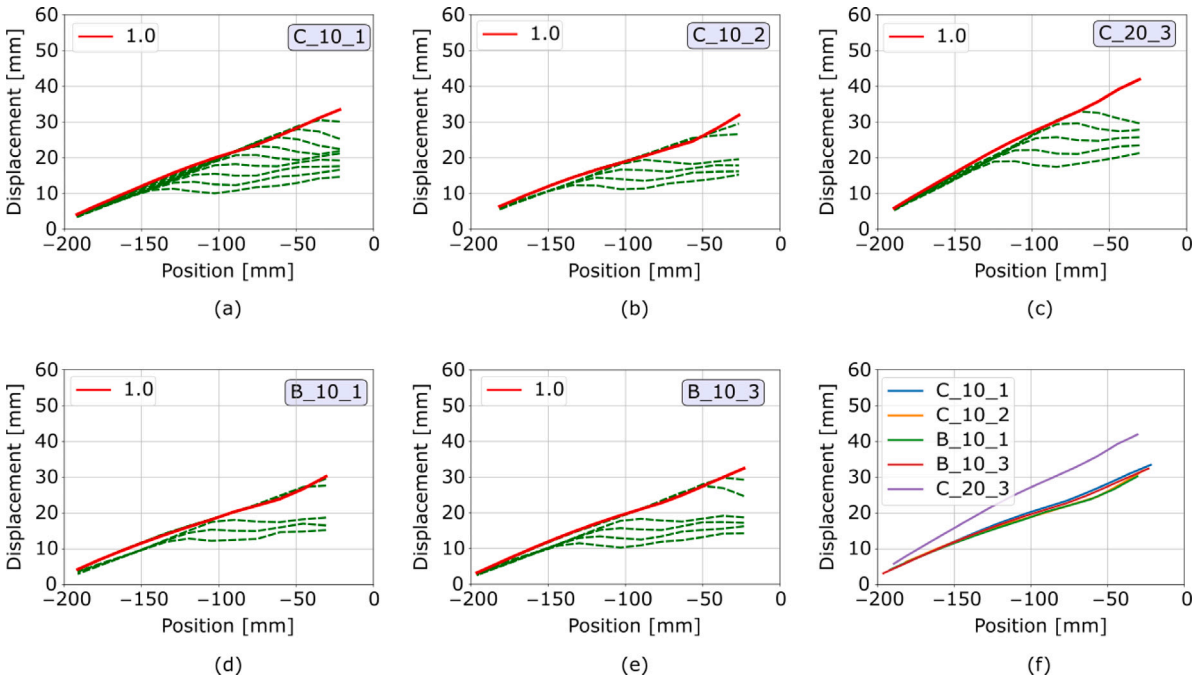

Fig. 10. All available deformation profiles for the airblast experiments on target plates with pre-cut defects in (a–e). The test identity is indicated in the upper right corner of each sub-figure. In (f), the deformation profile at maximum displacement are plotted together for all tests in (a–e) for comparison. It is noted that the deformation profiles of the C and B geometry consists of only one side of the plate center, due to issues with the fireball coming through the center.

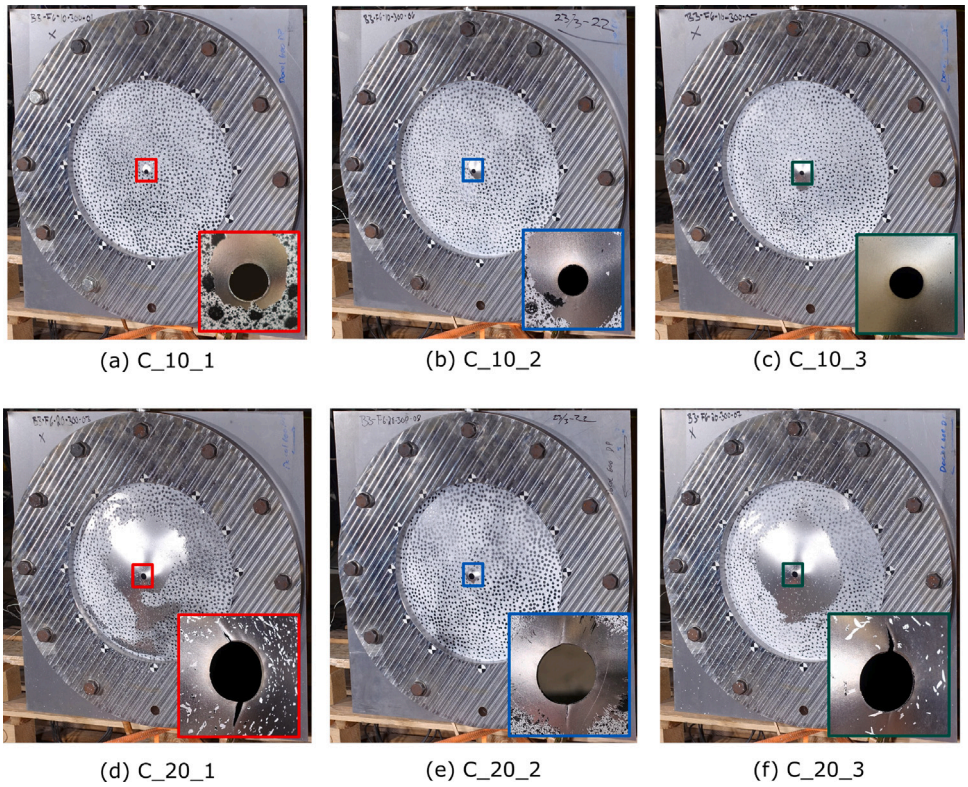

Fig. 11. Post images of all airblast tests on target plates with the C geometry. The test identity indicating the charge mass and repetition is given in the sub-captions. An additional zoomed image around the pre-formed hole is given at the lower right corner of each sub-figure.

the pre-cut hole (C) and ballistic hole (B) geometries, in an attempt to validate the repeatability in the loading conditions. Because of the fireball coming through the pre-formed defects, the deformation profiles are only obtained at one side of the plate center. Some images were also discarded, which is seen as fewer green lines indicating the plate movement.

Out of the 12 airblast tests on target plates with pre-formed holes, only 5 are presented in Fig. 10. For the remaining 7 experiments, the high-speed images were either too affected by the light from the fireball, or suffering from detachment of spray paint. All available deformation profiles are given in Fig. 10(a–e), while Fig. 10(f) gives a comparison of all deformation profiles at maximum displacement. It is observed that the deformation response for the C and B geometries follows trends similar to those for the FP geometry in Fig. 9. For the comparison of all deformation profiles at maximum displacement, only minor variations are seen. Thus, the results indicate that the loading conditions from the detonations are comparable for the repetitions within each of the two charge masses, and that the repeatability between tests with the same charge mass was good.

3.3. Fracture resistance

Figs. 11 and 12 show the permanent deformed configuration of the C and B geometries, respectively. The charge mass and repetition of each test are given in the sub-captions. No image sequences were made from these tests due to the challenges with the fireball dominating the high-speed images in the area of interest. From the images in Fig. 11(a–c), it is clear that none of the three repetitions of the C_10 configuration experienced any signs of fracture or localized necking around the pre-cut circular hole. As the charge mass was increased to 20 g in Fig. 11(d)–(f), all three repetitions resulted in small arrested cracks from the periphery of the circular holes. The crack lengths were measured to be 5.6 mm and 7.3 mm for C_20_1, 7.3 mm for C_20_2, and 6.1 mm and 4.9 mm for C_20_3. It is also noted that all cracks for the C_20 configuration propagated in the vertical direction only. As all target plates are mounted with the rolling direction vertically, the results indicate that the crack resistance is the lowest 90° to the rolling direction. This corresponds to the 90° material curves in Fig. 5.

The findings in the tests with the B geometry confirm the observations in previous studies [19], where the B geometry showed a reduced fracture resistance during blast loading compared to the C geometry (Fig. 12). In fact, it is seen that even at the 10 g charge mass, all three repetitions experienced crack initiation in some of the initial petalling cracks (see Fig. 12(a–c)). For the 20 g charge mass, all three B_20 tests resulted in large arrested cracks (see Fig. 12(d–f)). The material around the arrested cracks experienced large plastic deformations, where the petals around the pre-formed holes were bent outward. This final state of plastic deformation made it difficult to measure the arrested crack lengths. Instead, the largest measured distance between two crack tips

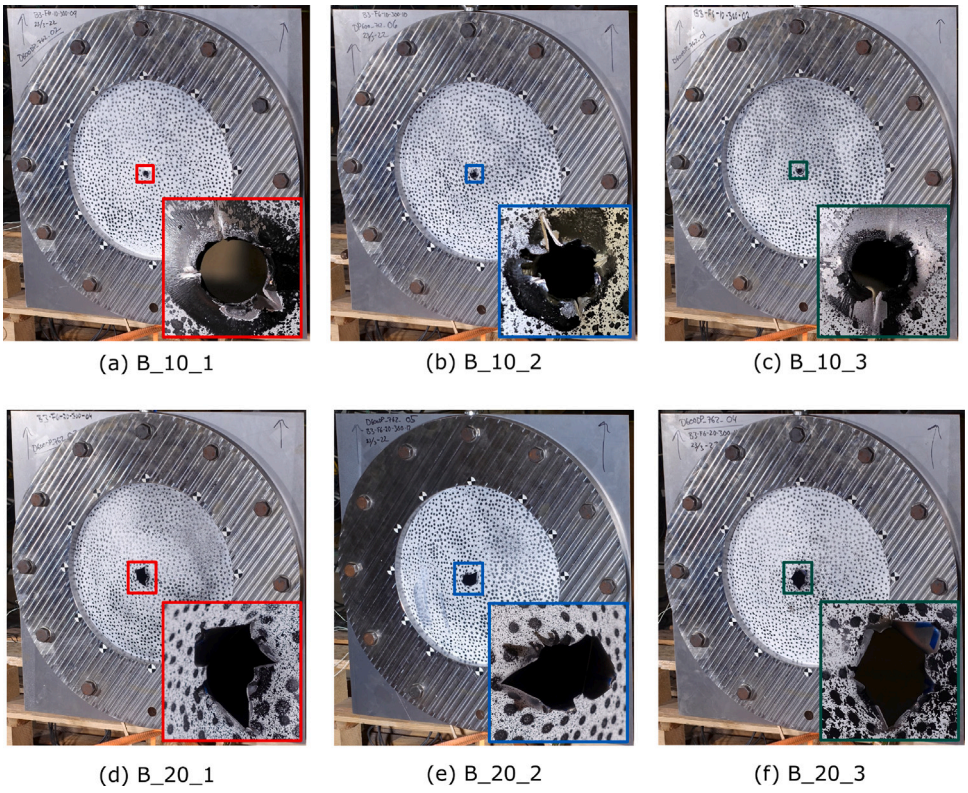

Fig. 12. Post images of all airblast tests on target plates with the B geometry. The test identity indicating the charge mass and repetition is given in the sub-captions. An additional zoomed image around the pre-formed hole is given at the lower right corner of each sub-figure.

was measured across the ballistic hole. For comparison, this was also done for the C geometry, and all measurements are given together with the pressure measurements in Table 2. By comparing the C and B geometries for the 20 g charge, it is seen that the B_20 tests experienced approximately twice as large cracks as the C_20 tests. For the change in charge mass from 20 g to 10 g for the B geometry, the crack lengths were reduced by almost a factor of 4. It should however be noted that non of the arrested cracks extended outside the local dome of plastic deformation at the center of the blast-loaded target plates. The largest measured distance between crack tips was 47.2 mm for the B_20_1 test, and this only covers 12% of the 400 mm diameter blast-exposed area of the target plates.

Because of the fireball passing through the pre-formed hole in the target plate, it is difficult to accurately evaluate crack propagations during the first 3–4 ms after the detonation. However, the extent of the cracks occurring at maximum displacement around 1 ms after the detonation seems to have a similar extent to the final arrested cracks when the plates are at rest.

4. Numerical work

All numerical simulations in this study were performed using the explicit finite element code LS-DYNA. Two different approaches for the modeling of explosives and air were tested and compared. That is, the Particle Blast Method (PBM) [42] and an Arbitrary Eulerian Lagrangian (ALE) approach [15,31,40–42]. The two different modeling techniques are briefly described in Sections 4.3 and 4.4.

The findings of the blast experiments in Section 3 indicated that the majority of both plastic deformations and crack propagation occur during the first millisecond after detonation. This was also confirmed by initial numerical simulations, and the numerical results in this section mainly focus on the response during 1–1.5 ms after the detonation.

4.1. Material modeling of the target plates

The Docol 600DP material used in the blast-loaded steel plates was modeled using *MAT_107, which is an elastic-thermoviscoplastic constitutive relation formulated through the modified Johnson-Cook relation as described in Ref. [52], and given in Eq. (2).

$$\sigma_{eq} = (A + R(p))\left(1 + \dot{p}^*\right)^c \left(1 - T^{*m}\right) \tag{2}$$

Table 2
Summarizing the peak values of the pressure measurements at the sensors P11 and PR2 for the blast tests on deformable steel plates. The given crack lengths represent the largest distance between two crack tips across the pre-formed hole.

Test	Repetition #	P11 [MPa]	PR02 [MPa]	Crack length [mm]
FP_10	1	0.594	0.054	No cracks
C_10	1	0.667	0.052	No cracks
	2	0.726	0.048	No cracks
	3	0.603	0.050	No cracks
B_10	1	0.615	0.052	12.7
	2	0.770	0.049	13.3
	3	0.699	0.049	20.6
FP_20	1	1.494	0.084	No cracks
C_20	1	–	–	25.8
	2	1.278	0.075	21.1
	3	1.095	0.075	23.9
B_20	1	1.701	0.076	47.2
	2	1.242	0.075	45.1
	3	1.085	0.075	44.5

Table 3
Parameters for the constitutive relation described in Eqs. (2)–(4). The strain rate sensitivity parameter, c, and the thermal exponent, m, are both taken from [11].

A [MPa]	Q_1 [MPa]	C_1 [–]	Q_2 [MPa]	C_2 [–]	c [–]	m [–]	W_c [MPa]	T_0 [K]	T_m [K]	T_c [K]
431.2	195.434	42.137	455.018	2.558	0.01	1.0	606.6	293	1800	1600

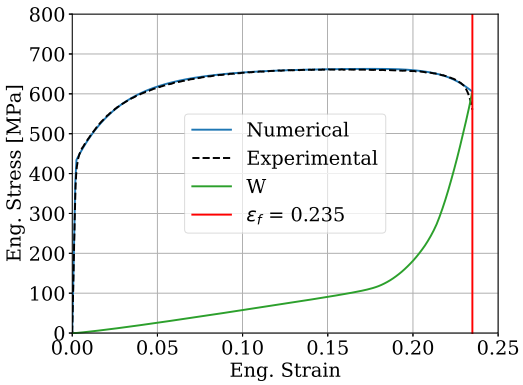

Fig. 13. Comparison of numerical and experimental stress–strain curves to fracture. The fracture parameter W_c was determined at the engineering fracture strain observed in the experiments, and is indicated with ε_f.

where σ_{eq} denotes the equivalent stress given by a von Mises yield surface, A the initial yield stress, and $R(p)$ the plastic strain hardening given in Eq. (3). The dimensionless plastic strain rate is given by $\dot{p}^* = \dot{p}/\dot{p}_0$, where the reference strain rate is given by $\dot{p}_0 = 5.0 \cdot 10^{-4}$ s^{-1}. The strain rate sensitivity of the material is accounted for by c, and the last term in Eq. (2) determines the temperature softening of the material. Here, $T^* = (T - T_0)/(T_m - T_0)$, where T_0 is a reference temperature and T_m is the melting temperature of the material. The temperature development in the material was accounted for by including adiabatic heating effects.

$$R(p) = \sum_{k=1}^{2} Q_k \left(1 - e^{-c_k p}\right) \tag{3}$$

In Eq. (3), Q_k and c_k are the material parameters of the Voce hardening law, and p denotes the equivalent plastic strain. The modeling of fracture was done through the Cockcroft–Latham (CL) fracture criterion [53], given in Eq. (4) as

$$D = \frac{W}{W_c} = \frac{1}{W_c} \int_0^p \langle \sigma_1 \rangle dp, \qquad \langle \sigma_1 \rangle = \max(\sigma_1, 0) \tag{4}$$

Here, D denotes the damage indicator and W_c is the critical fracture parameter. Fracture initiates when W reaches W_c, i.e., when D=1.0. Additionally, elements are also eroded if the temperature increase from adiabatic heating reaches the user defined critical temperature, T_c. Both the plastic strain hardening parameters Q_k and c_k, and the fracture parameter, W_c were calibrated through

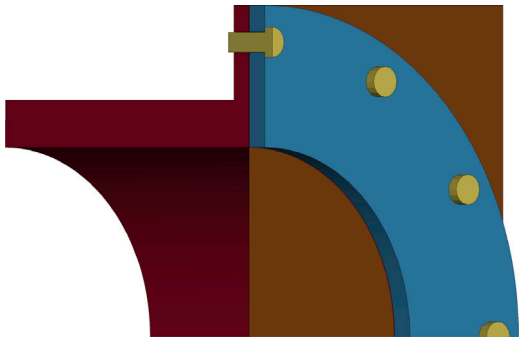

Fig. 14. The numerical model of the target plate, the confinement tube, and the clamping assembly, utilizing quarter symmetry for all parts.

an inverse modeling approach of the uniaxial tension tests to fracture. The tension test specimen was discretized using 0.8 mm shell elements, equal to the thickness of the specimen. The calibrated material parameters are summarized in Table 3, and the corresponding numerical engineering stress–strain curve is given and compared to the experimental curve in Fig. 13.

4.2. Discretization and boundary conditions — solids

To accurately describe the petalling failure mode of the thin plates during ballistic impact, a fine discretization with several solid elements across the 0.8 mm plate thickness is required. However, both of the blast modeling techniques, PBM and SALE, are computationally demanding. As a trade-off between the accuracy in the description of the structural response and the CPU costs, it was decided to apply shell elements with an in-plane element size equal to the 0.8 mm thickness for all plate geometries. The clamping frame, the bolts, and the confinement tube were modeled using solid elements. For simplicity, all structural parts applied the material model as described in Section 4.1. The boundary conditions for the bolts were applied similarly as in Ref. [11]. That is, the bolt tightening force was represented as a constant pressure applied to the clamping frame in the area covered by the bolt head. The free ends of the bolts were fixed on the opposite side of the bolt head for translation in all directions. Lastly, quarter symmetry was applied, and the corresponding numerical model of the clamping frame and target plate is shown in Fig. 14. Since a restart analysis with the particle blast method (PBM) was not possible, the ballistic impact and the blast loading were applied in the same analysis for all simulations. The projectile was modeled with solid elements, a rigid material model, and an initial velocity of 900 m/s. A parametric study of the fluid domain indicated that the length of the confinement tube and the fluid domain could be shortened significantly without affecting the blast load. For numerical efficiency, the current models used a confinement tube length of two pipe radii (i.e., 400 mm).

4.3. Particle blast method (PBM)

The particle blast method (PBM) is governed by the *DEFINE_PARTICLE_BLAST keyword in LS-DYNA, and represents a pure Lagrangian description of the detonation product and the resulting blast load on the surrounding structure. The air particles are initialized with a total amount of kinetic energy corresponding to the internal energy of the air at atmospheric conditions. For the high explosive (HE), the full chemical energy release from the detonation is transferred to the HE particles as kinetic energy. At time t = 0 ms, all HE particles are frozen and tightly packed. At a given detonation time, the HE particles are activated based on the distance to the given detonation point and the given detonation velocity for the explosive material [44].

Each particle typically represents 10^{15}–10^{20} molecules. To model each molecule as its own particle would result in unrealistic computational costs, and memory requirements for a full scale model. The relationship between the number of HE particles (NPHE) and the number of air particles (NPAIR) was determined so it reflects the ratios of the molar mass between the HE and air. This was done using the formula in Eq. (5)

$$NPAIR = \left(\frac{MAIR}{MHE}\right) NPHE \tag{5}$$

where $MAIR$ denotes the mass of air within the modeled domain, and MHE is the mass of the explosive charge. The reference model applied for the PBM approach in this study used 80k particles for the HE and 2174k particles for the air domain. The convergence with respect to the number of particles was evaluated for the corresponding mid-point displacement of the target plates. Due to interaction issues between the solid elements and the air particles, the confinement tube was modeled using shell elements. As no contact definition is required between the clamping frame and the particles, this was modeled in the same way as given in Section 4.2. As the inclusion of air particles impose a pressure of 1 atm, the air filled domain has to extend across both sides of the target plates to avid an artificial overpressure inside the confinement tube. Ambient boundary conditions were applied to the boundaries of the air domain, which means that only particles representing a pressure higher than 1 atm are allowed to translate across the boundary.

4.4. Arbitrary Eulerian-Lagrangian (ALE) method

The ALE description of the partially confined detonation is based on a finite element formulation for both the structural and fluid domains. All fluids are formulated through an ALE description, while the structural domain is represented by a Lagrangian formulation.

It should be noted that LS-DYNA offers two different ALE solvers, the traditional Multi-Material ALE (MMALE), and a more recent formulation called Structured ALE (SALE). The main difference between the two alternative ALE approaches is the discretization of the fluid domain. In MMALE, the fluid mesh is designed by the user in a similar way as for structural parts, without any restrictions on the shape of the mesh. In SALE, the meshing of the fluid domain is simply defined in the keyword-file, and the mesh is generated during the initialization of the model. Here, the mesh has to be structured, i.e., it has to take the shape of a rectangular box, containing only rectangular elements. As both the shape and varying element sizes within the fluid domain tend to affect the corresponding solution, the new meshing restrictions remove some of these uncertainties away from the user. Another difference between MMALE and SALE is the FSI algorithm used to enforce the interactions between the structural and fluid domains. For the MMALE models, several keywords need to be defined for the contact handling and leakage issues. In SALE, these options are removed, and the majority of contact options are determined automatically by the solver and defined by the keyword *STRUCTURED_FSI. In this study, it was decided to only consider the more recent SALE solver.

The fluid domain consists of two separate materials, i.e., the air and the detonation products. Both materials flow through the same fluid mesh, but they are not allowed to mix. The expansion of the detonation product leads to compression of the surrounding air and hence to an increase in pressure. The air was represented with the *LINEAR_POLYNOMIAL equation of state (EOS) expressed in terms of a perfect gas given by Eq. (6)

$$P = (\gamma - 1)\frac{\rho}{\rho_0}E, \qquad \gamma = \frac{C_p}{C_v} \tag{6}$$

where C_p and C_p are defined as the specific heat capacities under constant pressure and volume, respectively. As γ, E, and ρ_0 are all considered material constants, volumetric changes is the only contributor to the pressure change in this EOS. The pressure–volume relation for the expansion of the detonation product is governed by the Jones–Wilkins–Lee (JWL) EOS. Here, the relationship between pressure, P, volume V, and energy E is given by Eq. (7) as

$$P_{\mathrm{JWL}} = A\left(1 - \frac{\omega}{R_1 V}\right)e^{-R_1 V} + B\left(1 - \frac{\omega}{R_2 V}\right)e^{-R_2 V} + \frac{\omega E}{V} \tag{7}$$

where A, B, R_1, R_2, and $\omega = \gamma - 1$ are material parameters linked to the type of explosive material. The first two terms in Eq. (7) represent the rapid pressure drop in the detonation products from the expansion of the initially hot gases. The third and last term describes the behavior of an expanding ideal gas.

The detonation of the explosive material was initiated at the specified detonation point given by *INITIAL_DETONATION. During the initialization of the model, the air was governed by the EOS in Eq. (6) at atmospheric conditions. The explosive material is initially filled into the fluid domain as a un-detonated sphere with zero pressure and its solid state density ($\rho_{\mathrm{C-4}}$). The detonation of the explosive material is dealt with by *MAT_HIGH_EXPLOSIVE_BURN. Two alternative burn fractions are calculated based on the initial density of the un-detonated explosive, $\rho_{\mathrm{C-4}}$, the detonation pressure (Chapman–Jouguet pressure), P_{CJ}, and the detonation velocity, D. F_1 corresponds to a programmed burn and F_2 to a beta burn. The effective burn fraction for each element is always taken as the maximum of F_1 and F_2, i.e.,

$$F_1 = \begin{cases} \frac{2}{3}\left(\frac{A_{max}}{v_e}\right)(t - t_1)D, & t > t_1 \\ 0, & t \le t_1 \end{cases} \tag{8}$$

$$F_2 = \frac{1 - V}{1 - V_{CJ}}, \qquad V_{CJ} = 1 - \frac{P_{CJ}}{\rho_{C-4}D^2} \tag{9}$$

$$F = \max(F_1, F_2) \tag{10}$$

The pressure at any time is given by the EOS for the detonation products, P_{JWL}, scaled by the burn fraction, F, as given in Eq. (11). Thus,

$$P = P_{\mathrm{JWL}}F \tag{11}$$

The lightning time for an element, t_1, is based on its distance to the defined detonation point and the detonation velocity. v_e is the volume of an element and A_{max} the maximum projected area of the element. As an element approaches $F = 1.0$, F is fixed and the pressure is determined solely by the EOS. If F exceeds 1.0, it is reset to 1.0. In principle, this means that the detonation of the explosive is based on either the passing of the detonation wave (F_1), or by volumetric compression (F_2), where the first criterion to reach unity decides. The material parameters applied for the air and the explosive are taken from Ref. [44], and are given in Table 4.

Table 4
Material parameters applied for C-4 and air. All parameters are taken from [44]. It is noted that $E_0 = P_0/(\gamma - 1)$.

High explosive - C-4								Air			
ρ_{C-4} [kg/m^3]	D [m/s]	P_{CJ} [MPa]	A [MPa]	B [MPa]	R_1 [–]	R_2 [–]	ω [–]	ρ_0 [kg/m^3]	γ [–]	P_0 [MPa]	E_0 [MPa]
1601	8190	28 000	597 400	13 900	4.5	1.5	0.32	1.225	0.4	0.1	0.25

4.4.1. Advection method

The re-mapping in the ALE methods involves transfer of state variables from the deformed Lagrangian configuration back to the undeformed mesh. The particular advection algorithm is chosen by the user. Several methods are available and governed by the "METH" keyword in *CONTROL_ALE. LS-DYNA recommends METH=-2 in combination with *MAT_HIGH_EXPLOSIVE_BURN. This choice represents a Van Leer advection scheme where the state variables are assumed to vary with a higher order interpolation function internally in each element for the advection calculations. This gives an advection scheme with second-order accuracy, which is also stated to better preserve the interface of materials described by *MAT_HIGH_EXPLOSIVE_BURN in certain conditions [54].

In this study, it was decided to apply the recommended advection method, "METH=-2" for the reference model, and all ALE elements are formulated with element formulation 11. This represents a one-point ALE multi-material element. However, an alternative advection method was tested, and the corresponding results are given in Appendix.

4.5. Numerical results

As a benchmark for the SALE model, the reflected pressure histories were compared at the same locations as P01 and P02 in the ballistic pendulum tests (see Figs. 4 and 7). Additionally, the force acting from the fluid onto the pendulum was evaluated, and denoted "FSI force". This force is governed by the keyword *DATABASE_FSI, and is defined as the averaged total estimated coupling force along the global coordinate directions between a given Lagrangian surface entity and the fluids. Both the pressure and force histories are presented in Fig. 15. For the PBM simulations, some difficulties were encountered with respect to the modeling of surrounding air particles, and the interaction with structural parts when modeled with solid elements. That is, air particles were filled both around and inside all structural parts, resulting in artifacts and non-physical behavior. This problem was most evident in the modeling and simulation of the ballistic pendulum tests. As a consequence, the PBM simulations were only evaluated based on the experimental findings in tests involving the deformable steel plates.

Fig. 15 shows that the main trends from the experimental observations are captured in the SALE simulations. For P02, the initial and the second pressure peaks are occurring at similar times and are of a comparable magnitude numerically and experimentally. The numerical measurements at pressure sensor P01 experienced significant oscillations and amplified magnitudes compared to the experiments, especially for the second pressure peak. Due to the symmetry in the model, this sensor lies at the border of the two symmetry planes, and at the blast-exposed surface of the pendulum. A possible explanation for the unstable measurements at this point could be that the air element at this position represents the most constrained element in the entire model. As the reflected pressure builds up, the two fluids are trapped between three reflective planes. It should also be noted that the fluid domain consists of two materials, the HE and the surrounding air. Each finite element may then contain both materials, which are described by two separate EOS. The numerically sampled pressure represents the volume weighted pressure of the two fluids at the given location. Rapid changes in volume fractions and pressure could also possibly affect the pressure histories. However, the corresponding total force seems to remain stable through the entire event, despite the oscillating pressure histories at the P01 location. The corresponding pressure fields and log files from the simulations do not indicate any instabilities either.

The effect of fluid element size was evaluated both with respect to the pressure measurements at P01 and P02 on the blast exposed surface of the pendulum, and with respect to the mid-point displacements of the deformable steel plates. An element size of 1.25 mm was found to give sufficiently converged predictions. Only minor improvements were observed for a further refinement to 1.0 mm air elements. However, the computational time increase rapidly with a decreased element size, and the 1.25 mm mesh was therefore applied in the simulations of the deformable steel plates in Section 4.5.1.

4.5.1. Deformable steel plates

As the pendulum was replaced by deformable steel plates, discretized by 0.8 mm shell elements, pressure and material leakage became an issue. By increasing the penalty factor in the FSI contact the simulations showed a strong trade-off between leakage and stability. Different contact and penalty factor definitions were tested, but ultimately it was decided to accept some leakage in the models.

Since there are no real alternative for experimental techniques capable of measuring surface pressures acting on thin plates undergoing large deformations, the numerical results were used in an attempt to better understand the loading conditions. That is, three additional pressure sensors were defined in the simulations together with the previously evaluated sensors P01 and P02. The three additional sensors are named P50, P100, and P200, and placed 50 mm, 100 mm and 200 mm away from the plate center at the blast-exposed area. This means that the initial blast-exposed area is now covered with five pressure sensors between the center and the confinement wall, with a distance of 50 mm between each sensor. The position of the numerical sensors is indicated in Fig. 16(a). The corresponding pressure histories for the simulation of test FP_20 are given in Fig. 16(b).

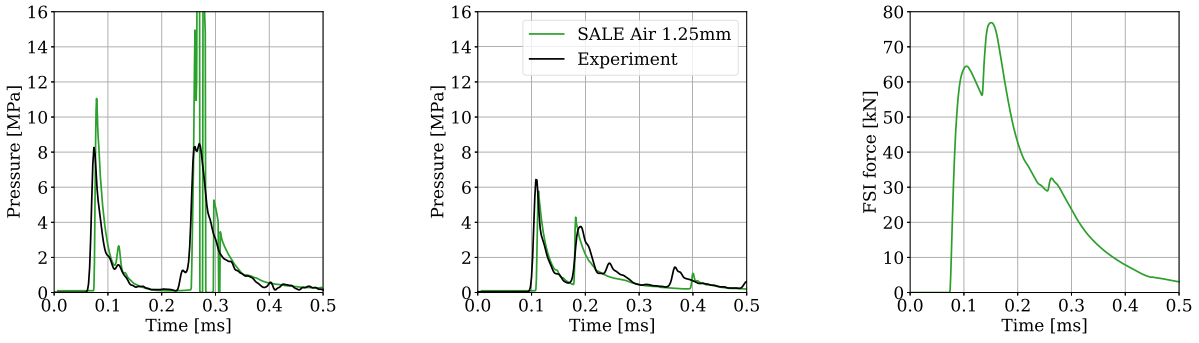

Fig. 15. The recorded pressure histories from pressure sensors P01 and P02 compared to the experimental observations for the SALE simulations in (a) and (b) for the pendulum test detonating 20 g of C-4. The corresponding total force history is given in (c). The applied element size for the fluid domain is indicated in the legend.

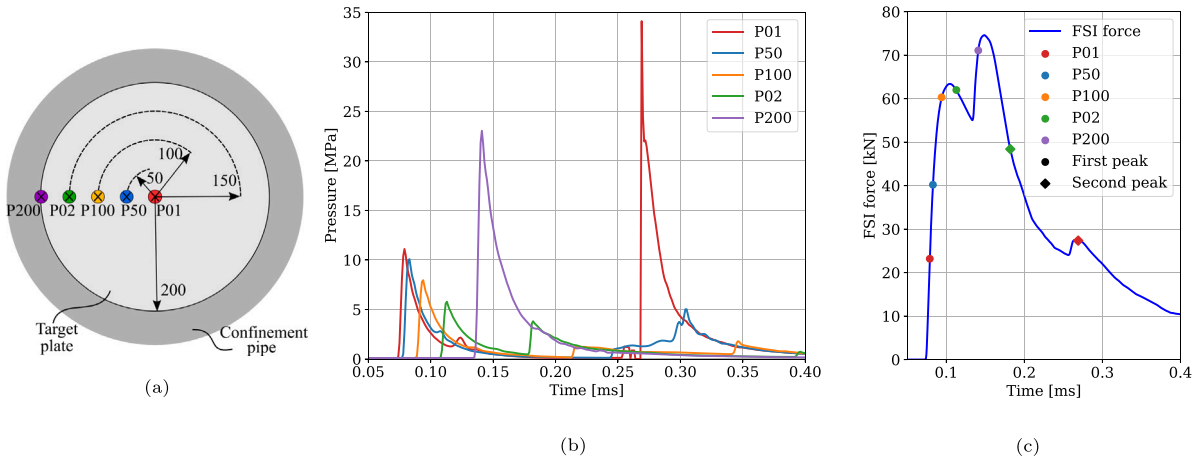

Fig. 16. Positioning and naming conventions of numerical pressure sensors are shown in (a). The corresponding pressure histories for the FP_20 simulation and the total force are given in (b) and (c). For the total force plot in (c), the times for the pressure peaks of each sensor in (b) are indicated with the dots on the graph. The color of the dots follow the same color convention as in the pressure plots in (a), as indicated in the legend box.

Based on the pressure histories at the five sensors in Fig. 16(b), it is observed that all five sensors have its own distinct pressure history. That is, an initial peak pressure followed by an exponential decay. P01 was located at the target plate center and experienced the lowest arrival time and the highest initial peak pressure. As expected, an increasing distance from the sensor to the plate center results in an increase in the time of arrival increased and a decrease in the magnitude of the initial pressure peak. This trend was however with one exception. The pressure sensor placed in the corner between the target plate and the confinement tube experienced an initial pressure peak significantly higher than the other four.

To better understand the spatial and temporal pressure distributions, the numerically obtained pressure fields at six selected times are shown in Fig. 17. As the explosive charge is placed exactly one tube radius away from the target plate, the reflections from the tube wall reaches the corner simultaneously as the reflections from the target plate, which causes an amplification of the reflected pressure. This is shown in Fig. 17(b) and (c). The reflected pressure at the corner then starts to travel along the target plate back towards the center of the target plate, as indicated with the secondary peaks recorded at P02, P100, and also at P50 (see Fig. 16(b)). The secondary peaks are decreasing rapidly with respect to the distance from the corner, and it is observed that they coincide with the decay in the pressure history of P200 in Fig. 16(b). The largest peak pressure throughout the entire blast loading event occurred for the secondary peak at the plate center, i.e., at P01. A strong focusing effect of the pressure develops as the reflections from the tube wall propagating towards the center line of the confinement tube and starts to interact with the reflections from the target plate, as seen in Fig. 17(c–e).

The pressure measurements in Fig. 16(b) only describes the pressure histories at discrete points across the blast-exposed area of the target plates. To relate the pressure histories to the corresponding total force on the target plates, the total force is plotted in Fig. 16(c), where the pressure peaks of all numerical pressure sensors are indicated. Here, it is seen that the force history contain three force peaks, two major peaks, and one minor.

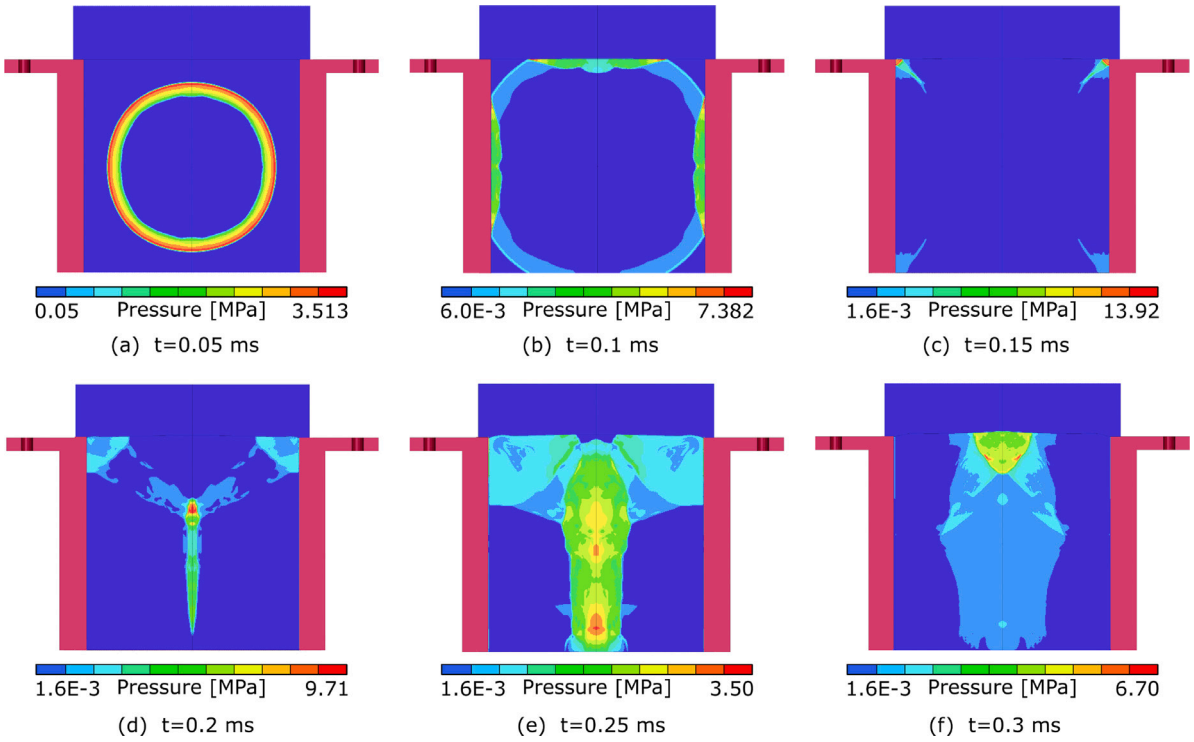

Fig. 17. Numerically obtained pressure fields at six selected times for the simulation of test FP_20. The time for each pressure field is given in the sub-caption. The deformable steel plate is seen as the thin horizontal line at the upper end of the tube.

The initial rise in force was obviously caused by the first pressure wave impacting the target plate, which occurred about 0.075 ms after the detonation. The maximum force during the first peak was reached at 0.105 ms, which is in-between the first pressure peak at sensors P100 and P02 in Fig. 16. This is also very close to the pressure field given in Fig. 17(b).

The second and largest force peak started to increase at 0.135 ms, which coincides perfectly with the initial rise in pressure at sensor P200 in Fig. 16. The local maximum for the second force peak occurred at 0.15 ms, placing it between the initial pressure peak at P200 and the secondary pressure peak at P02. With respect to the pressure fields in Fig. 17, the second peak occur between (b) and (d). The magnitude of the second force peak suggests that the largest force transfer between the fluid and the structure takes place closer to the confinement wall than the plate center.

The third and smallest force peak was initiated at 0.26 ms, i.e., during the local focusing effect of pressure around the plate center. This is when the major pressure peak for P01 occurred in Fig. 16. It is however interesting that the lowest peak force corresponds to the highest measured pressure during the entire blast loading event. This indicate that the focusing effect of pressure only covers a small area, as it induces a small force.

For the evaluation of the corresponding global deformations in the steel plates without pre-formed defects (FP), both the midpoint displacements and deformation profiles are presented in Figs. 18 and 19. The midpoint displacements are presented for both FP_10 and FP_20, while the corresponding deformation profiles are only given for FP_20. As no pressure fields were available for the PBM simulations, the structural response was the best available comparison between the experiments and the SALE and PBM simulations.

The midpoint displacements in Fig. 18 showed similar trends for both FP_10 in (a) and FP_20 in (b) for the comparison between PBM, SALE and the experimental results. The predictions from the PBM simulations resulted in larger displacements than the experiments, while the SALE simulations resulted in smaller displacements than the experiments. Moreover, the SALE simulations resulted in varying deformation rates up to maximum displacement, similarly to what was found in the experiments. The PBM simulations resulted in almost linearly increasing deformations with a slightly increased deformation rate closer to the maximum displacement.

The observed differences in midpoint displacement rates between the PBM and SALE approaches could be explained by the corresponding deformation profiles in Fig. 19. For the SALE simulations in (a), the center portion of the plate is deforming the fastest for the first 0.45 ms. After this point, the plastic hinge starts to move faster than the mid-section, and at 0.75 ms the mid section experienced smaller out-of-plane deformations than the plastic hinge. From this point and up to maximum displacement, the deformations mainly take place at the mid-section of the plate, resulting in the increased midpoint displacement rate seen in Fig. 18(b). The deformation profiles from the PBM simulation experienced a much more distinct plastic hinge with a relatively flat mid-section (Fig. 19(b)). This is also closer to what one would expect from a thin plate exposed to a uniform and impulsive loading (see e.g., Ref. [55]). This could also indicate that the loading conditions from the PBM simulations give a more uniform distribution

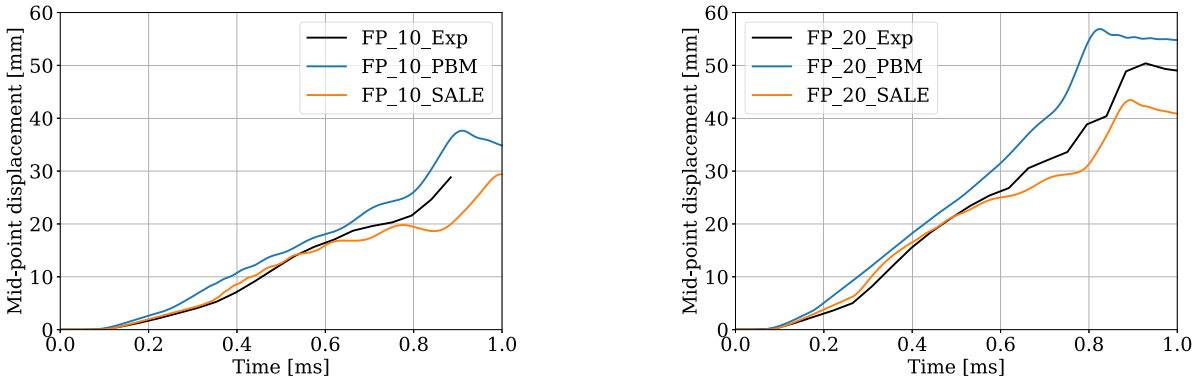

(a) (b)

Fig. 18. Midpoint displacement histories for FP_10 in (a) and FP_20 in (b). In both plots, the simulation results from PBM are compared to SALE and the experimental observations. As previously mentioned in Section 3, midpoint displacement from the FP_10 experiment was not recorded all the way up to the maximum displacement due to detachment of the spray paint.

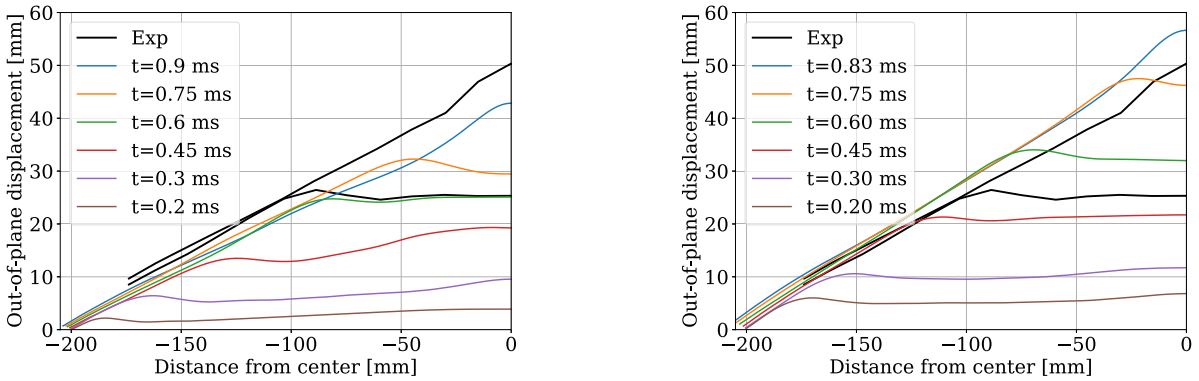

(a) SALE (b) PBM

Fig. 19. Deformation profiles for FP_20 obtained from the SALE simulation in (a) and the PBM approach in (b). The deformation profiles are plotted at selected times which are given in the legends for each sub-figure. The experimentally obtained deformation profiles at maximum deformation and 0.5 of maximum from Fig. 9 are included in both plots with black and labeled "Exp".

across the blast-exposed area of the target plates than the more advanced SALE simulations. This assumption is however hard to justify, as the total force histories between the plate and the particles experienced significant oscillations.

To sum up the comparison of the structural response, the PBM simulations ended with approximately 10% larger displacements than the experiments, and the SALE simulations with approximately 10% lower displacements than the experimental findings. The leakage observed in the SALE simulations is assumed to be part of the reason for the underestimation of the deformation response. At about 0.3 ms after the detonation, right after the second pressure peak at the center of the plate, some of the HE material started to flow through the center of the target plate in the SALE simulations. Leakage occurred only for the shell elements and the tube did not experience leakage in any of the simulations. It is also noted that no leakage occurred in the pendulum simulations, even though the contact formulation was identical to the one for the target plates. This motivated one simulation of test FP_20 using solid elements for the target plate, to investigate whether the leakage issue was related to the element formulation. This did not solve the leakage problem, which seems to be related to the small thickness of the target plate. This is however not confirmed, and require further numerical investigation. Such investigations are considered beyond the scope of this work.

4.5.2. Fracture resistance

The numerically predicted fracture resistance in the different models reflects the findings of the global deformation response in Section 4.5.1. Hence, the SALE approach underpredicts the dynamic response for the FP geometry. Interestingly, the SALE simulations failed to predict fracture for the C and B geometries. The PBM approach overpredicted the dynamic response to such an extent that it was able to predict fracture for both the C_20 and B_20 tests. The numerically obtained damage fields from C_20_PBM,

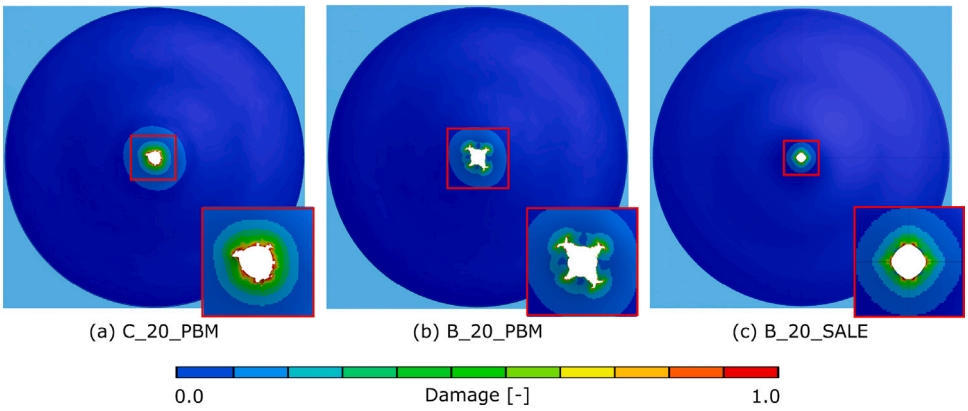

Fig. 20. Numerically obtained damage fields and arrested cracks for (a) C_20_PBM, (b) B_20_PBM and (c) B_20_SALE. The identity of each simulation is given in the sub-caption. All three field maps were sampled right after the instant of maximum displacement.

B_20_PBM and B_20_SALE are given in Fig. 20. The field plot is represented as the CL-damage parameter from Eq. (4), and the images were sampled at the instant of maximum displacement.

The C_20_PBM simulation in Fig. 20(a) ended in several small cracks arrested around the pre-formed circular hole. The largest cracks were found in the B_20_PBM simulation, where four significant cracks occurred pointing towards the plate diagonals. The material between the arrested cracks was also deformed outward as in the experiments after the crack propagation was arrested. This is however not illustrated in Fig. 20, as the images were sampled at the initial maximum displacement. Even though the PBM approach overestimated the dynamic response, and most likely the impulse transfer from the detonation, the length of the arrested cracks in the C and B geometries were underestimated compared to the experiments. Similar to the findings in Elveli et al. [19], this confirms that the 0.8 mm shell elements are unable to predict an accurate fracture response during blast loading for the plates with pre-formed defects. For the B_20_SALE model with an additional underestimation of the loading from the detonation, no signs of fracture occurred in this simulation, as seen in Fig. 20(c). Here, the damage evolution around the ballistic impact hole ended at approximately half of the critical value to initiate fracture. As the charge mass was reduced to 10 g, none of the numerical simulations resulted in crack initiation. For the PBM simulations, the reduced fracture resistance in the B geometry compared to the C geometry was captured. Although the discretization of the target plate was too coarse to give a satisfactory representation of the ballistic impact event, cracks were initiated at the most damaged locations from the ballistic impact holes. The numerical models generally resulted in an overestimation of the fracture resistance compared to the experimental findings.

The findings in this work confirm the trade-off between computational (CPU) time and accuracy in the numerical modeling of combined ballistic impact and blast loading. That is, simulations of ballistic impact require a very fine discretization of the target plate to obtain reliable predictions, while blast simulations need to use a much coarser mesh to run within a reasonable computational time. This is challenging when modeling the combined effect of fragment impact and blast loading on plated structures, especially if a realistic fracture mode from the ballistic impact and a feasible CPU cost during the blast loading phase of the simulation are important.

4.6. Discussion on the performance of the SALE and PBM approaches in blast simulations

Based on the predictive capabilities of the PBM and SALE approaches, some important differences need to be discussed. Both the PBM and SALE models resulted in structural deformations with an approximate deviation of 10% relative to the experimental findings, meaning that the predictive capabilities are in the same order of magnitude. However, the PBM models overestimated the structural response, leading to comparable estimates of the fracture resistance during blast loading. On the contrary, the SALE simulations underestimated the experimental observations in terms of deformation response, resulting in non-conservative estimates of the fracture resistance.

Concerning the CPU cost, the two numerical approaches performed similar when running on the same amount of CPUs. It was however possible to run the PBM simulations on more CPUs than the SALE simulations without causing numerical issues during the massively parallel processing (MPP) domain decomposition in the initialization of the models. Hence, the PBM simulations may further reduce the total simulation time by increasing the number of CPUs. All PBM simulations presented in this study included both the modeling of the explosive charge and the surrounding air. The number of particles representing the explosive charge was responsible for less than 4% of the total amount of particles in the model. This means that most of the CPU efforts were occupied to describe the surrounding air particles. The importance in the modeling of the surrounding air is very case dependent, and the comparison of CPU costs between SALE and PBM may vary significantly for other applications.

Compared to the SALE approach, the PBM approach involves a more user-friendly procedure in the establishing the numerical model. The PBM in LS-DYNA requires less input, with only a few keywords governing the blast loading domain. There are no need for any additional EOS for the particle domain. However, a too coarse description in the number of particles, or a too large

time-step definition generally leads to an overestimation of the blast load and more conservative estimates of the structural response. On the contrary, a coarse mesh of the fluid domain in a SALE simulation distributes the shock across a larger area, leading to an underestimation of both the propagation of the shock and the pressure amplifications during interaction with its surroundings. The great advantage of a well-defined SALE model is the detailed description of the entire loading event, including both the pressure build-up and the effects of interactions with surrounding structures. The SALE models are superior compared to the simpler PBM approach for a more detailed understanding of the different mechanisms governing the fluid–structure interaction (FSI) during a confined detonation.

As both approaches have their strengths and weaknesses, it is challenging to generalize and favor one approach above the other. The advantages of the two modeling approaches come down to the problem at hand, and the desired output and requirements from the numerical simulations.

5. Concluding remarks

This study evaluates both experimentally and numerically the effect of complex, partially confined blast loads on thin steel plates with pre-formed defects resembling those from a fragment impact. Assuming that the fragment impacts before the blast wave, the blast resistance of plates with perforations from ballistic impacts (B) was compared to that of target plates containing idealized pre-cut circular (C) holes. The main conclusions from the study are as follows.

- The work succeeded in establishing robust and reliable experimental setups in controlled laboratory environments when assuming that the fragment impacts the target before the blast load.
- The work also succeeded in subjecting thin steel plates to more complex blast environments compared to previous studies using a shock tube to generate blast-like loading conditions. However, despite the distinct differences in the spatio-temporal distribution of the loading, the differences in the dynamic response between the applied plate geometries remains unchanged.
- The displacement profile across the blast-exposed area of the targets took the shape of a global dome with a superimposed local dome around the center of the plate. If no significant fracture occurred, the global deformations seems to be unaffected by the plate geometry.
- The plate geometries showed distinct differences in terms of fracture resistance during blast loading. As expected, target plates without pre-formed defects resulted in large plastic deformations without any signs of fracture for both charge masses. Target plates with pre-cut circular holes (C) experienced vertical arrested cracks for the largest charge mass, while target plates containing initial ballistic impact holes (B) experienced more and larger arrested cracks for both charge masses. For the B geometry, all arrested cracks were initiated at the initial petalling cracks from the ballistic impact holes.
- The SALE simulations were in good agreement with the measured pressure histories in the pendulum experiments. Some difficulties were encountered in the simulations of the steel plates, where leakage occurred during the last phase of the blast loading event. Compared to the experimental findings, the PBM simulations overestimated the dynamic response by approximately 10%, while the SALE simulations underestimated the deformations with a similar magnitude.
- The numerical models of the target plates can be used to gain more insight into the combined effect of ballistic impact and blast loading in partially confined detonations. Compared to previous studies performed in a shock tube, this study extends the validity of the models to also include load environments of localized, non-uniform pressure distribution.

Declaration of competing interest

The authors declare that they have no known competing financial interests or personal relationships that could have appeared to influence the work reported in this paper.

Data availability

Data will be made available on request.

Acknowledgments

This work has been carried out with financial support from the Research Council of Norway (RCN) through the Centre for Advanced Structural Analysis (CASA), Centre for Research-based Innovation (RCN Project No. 237885); the Norwegian Defence Estates Agency; and the Norwegian Ministry of Justice and Public Security.

Appendix. Advection method

The advection method represented by METH=3 has also been applied in studies on confined blast loading [20]. This method replaces the higher-order variations of state variables within each element in METH=2, to a constant value. This leads to a first order accuracy. Generally, it is not possible to conserve both the kinetic energy and the momentum during advection. METH=3 is formulated through the donor cell method, which expected to be more dissipative than the Van Leer method. To improve the

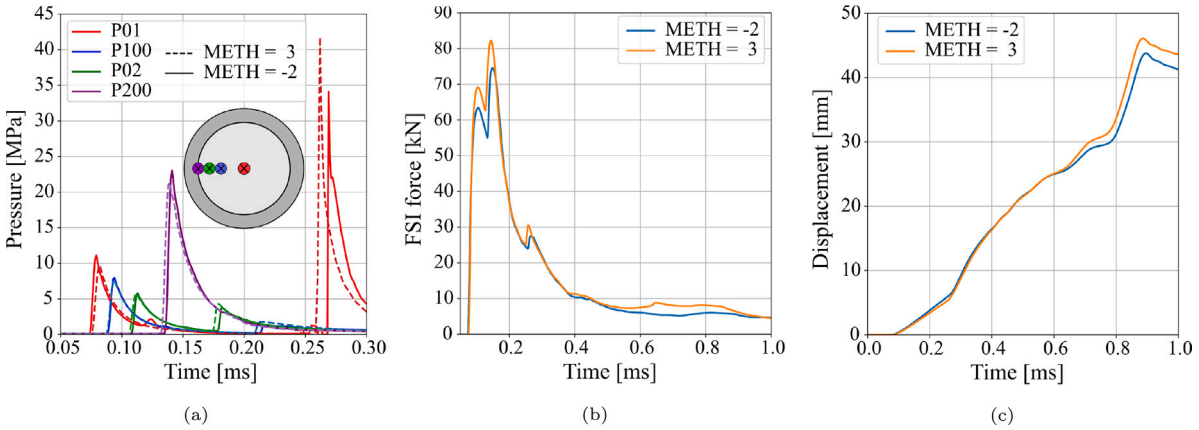

Fig. A.1. Comparison of two alternative advection methods, METH=-2, and METH=3, for the ALE domain. The pressure histories at a selection of pressure sensors are given in (a), the corresponding FSI force in (b), and the resulting midpoint displacements in (c). It is noted that the reference model for the numerical work in this study applied METH=-2. The two simulations represents the 20 g detonation.

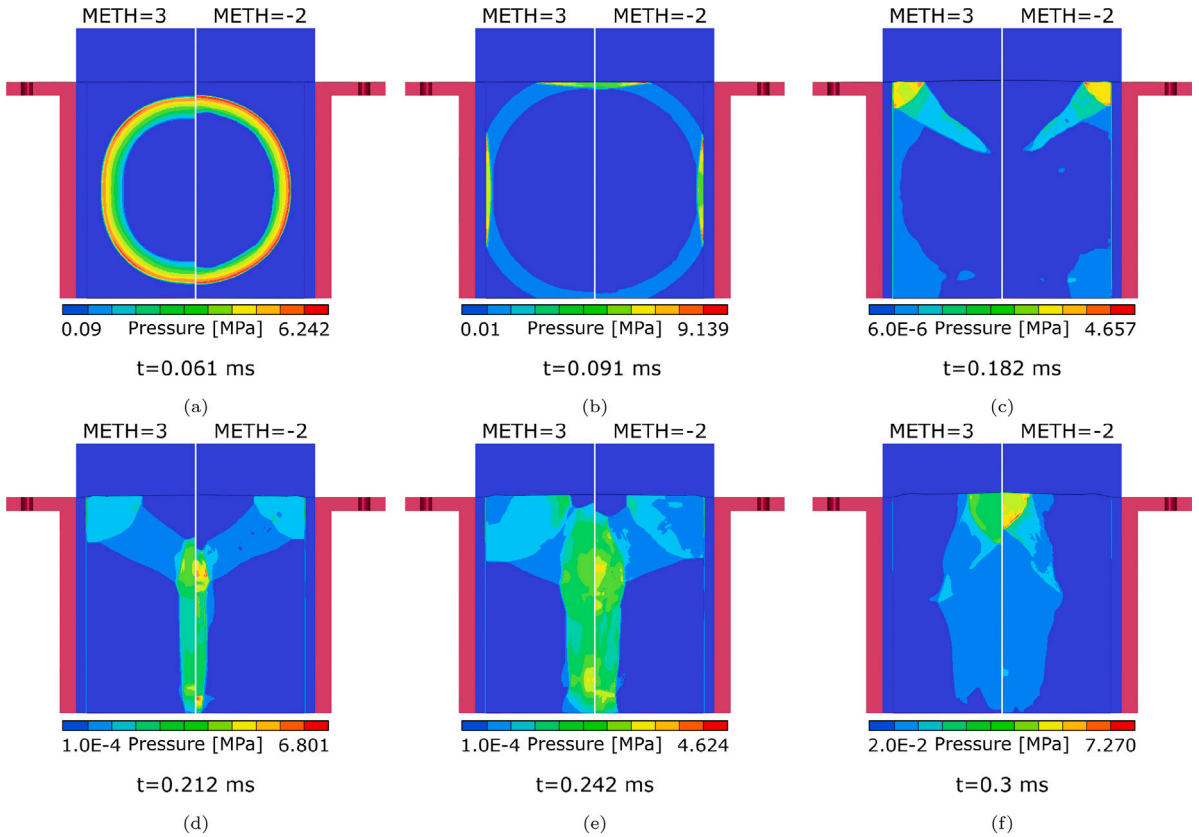

Fig. A.2. Comparison of the pressure field for the two advection methods. The two models are compared at six given times which are labeled for each subfigure. The two simulations represents the 20 g detonation.

conservation of energy, METH=3 additionally stores the loss of kinetic energy as increased internal energy during the advection step [54]. However, both methods apply the same algorithm for the re-mapping of node-specific variables.

The numerical pressure measurements at a selection of pressure sensors are plotted together with the corresponding FSI force and mid-point displacements for the comparison of the two alternative advection methods described in Section 4.4.1 are presented in Fig. A.1 and Fig. A.2. Only the 20 g detonation was considered. From the pressure measurements in Fig. A.1(a), it is seen that the incoming pressure is fairly similar for the two methods. The initial pressure peaks are somewhat smaller for METH=3, while the second pressure peaks after the interaction effects are slightly larger. A slight time-shift is also observed between the two methods, where the pressure peak from the interactions with the confinement occur earlier for METH=3 than for METH=-2. The corresponding FSI force and midpoint displacements are increased from METH=-2 to METH=3.

The obtained pressure fields for the two advection methods are compared in Fig. A.2. Here, the two models are aligned next to each other at six selected times during the blast simulations. For the initial shock propagation, it is seen that METH=3 gives a thicker shock front than METH=-2, while a slightly higher pressure is seen for METH=-2. Generally, it seems that METH=3 gives a slightly larger volume with high pressures than METH=-2. However, the effects of changing the advection method was not studied in any further detail than what presented in Figs. A.1 and A.2.

References

[1] J. Wei, M.S. Shetty, L.R. Dharani, Failure analysis of architectural glazing subjected to blast loading, Eng. Fail. Anal. 13 (7) (2006) 1029–1043.
[2] M. Kristoffersen, A. Minoretti, T. Børvik, On the internal blast loading of submerged floating tunnels in concrete with circular and rectangular cross-sections, Eng. Fail. Anal. 103 (2019) 462–480.
[3] S. Yao, D. Zhang, F. Lu, N. Zhao, Y. Li, Fast prediction method of failure modes for steel box structures under internal blast loading, Eng. Fail. Anal. 120 (2021) 104919.
[4] K.A. Marchand, M.M. Vargas, J.D. Nixon, The synergistic effects of combined blast and fragment loadings, Tech. Rep., Southwest Research Inst, San Antonio Texas, 1992.
[5] D.W. Hyde, U.A.E.W.E. Station, U.S.A.C. of Engineers, User's Guide for Microcomputer Programs ConWep and FunPro, Applications of TM 5-855-1, "Fundamentals of Protective Design for Conventional Weapons", Instruction report, U.S. Army Engineer Waterways Experiment Station, 1988.
[6] U. Nystrøm, K. Gylltoft, Numerical studies of the combined effects of blast and fragment loading, Int. J. Impact Eng. 36 (2009) 995–1005.
[7] X. Kong, W. Wu, J. Li, P. Chen, F. Liu, Experimental and numerical investigations on a multi-layer protective structure under the synergic effect of blast and fragment loadings, Int. J. Impact Eng. 65 (2014) 146–162.
[8] H.Y. Grisaro, A.N. Dancygier, Characteristics of combined blast and fragments loading, Int. J. Impact Eng. 116 (2018) 51–64.
[9] K. Rakvåg, N. Underwood, G. Schleyer, T. Børvik, O. Hopperstad, Transient pressure loading of clamped metallic plates with pre-formed holes, Int. J. Impact Eng. 53 (2012) 44–55.
[10] Y. Li, W. Wu, H. Zhu, Z. Wua, Z. Dub, The influence of different pre-formed holes on the dynamic response of square plates under air-blast loading, Eng. Fail. Anal. 78 (2017) 122–133.
[11] V. Aune, G. Valsamos, F. Casadei, M. Langseth, T. Børvik, On the dynamic response of blast-loaded steel plates with and without pre-formed holes, Int. J. Impact Eng. 108 (2017) 27–46.
[12] H. Granum, V. Aune, T. Børvik, O.S. Hopperstad, Effect of heat-treatment on the structural response of blast-loaded aluminium plates with pre-cut slits, Int. J. Impact Eng. 132 (2019) 103306.
[13] V. Aune, G. Valsamos, F. Casadei, M. Langseth, T. Børvik, Influence of fluid-structure interaction effects on the ductile fracture of blast-loaded steel plates, EPJ Web Conf. 250 (2021) 02019.
[14] W. Li, P. Wang, G. peng Feng, Y. gang Lu, J. zheng Yue, H. min Li, The deformation and failure mechanism of cylindrical shell and square plate with pre-formed holes under blast loading, Def. Technol. 17 (4) (2021) 1143–1159.
[15] C. Zhang, P. Tan, Y. Yuan, Confined blast loading of steel plates with and without pre-formed holes, Int. J. Impact Eng. 163 (2022) 104183.
[16] N. Gupta, Nagesh, Deformation and tearing of circular plates with varying support conditions under uniform impulsive loads, Int. J. Impact Eng. 34 (1) (2007) 42–59.
[17] Y. Yuan, P. Tan, Deformation and failure of rectangular plates subjected to impulsive loadings, Int. J. Impact Eng. 59 (2013) 46–59.
[18] V. Aune, E. Fagerholt, K. Hauge, M. Langseth, T. Børvik, Experimental study on the response of thin aluminium and steel plates subjected to airblast loading, Int. J. Impact Eng. 90 (2012) 106–121.
[19] B.S. Elveli, T. Berstad, T. Børvik, V. Aune, Performance of thin blast-loaded steel plates after ballistic impact from small-arms projectiles, Int. J. Impact Eng. (2023) 104437, http://dx.doi.org/10.1016/j.ijimpeng.2022.104437.
[20] O. Atoui, G. Kechagiadakis, A. Moumen, A. Maazoun, B. Belkassem, L. Pyl, D. Lecompte, An explosive driven shock tube-based laboratory scale test for combined blast and fragment impact loading, Appl. Sci. 12 (14) (2022).
[21] Y. Hu, C. Wu, M. Lukaszewicz, J. Dragos, J. Ren, M. Haskett, Characteristics of confined blast loading in unvented structures, Int. J. Prot. Struct. 2 (2011) 21–44.
[22] I. Edri, Z. Savir, V. Feldgun, Y. Karinski, D. Yankelevsky, On blast pressure analysis due to a partially confined explosion: I. Experimental studies, Int. J. Prot. Struct. 2 (1) (2011) 1–20.
[23] US Army Corps of Engineers (USACE), Structures to resist the effects of accidental explosions, UFC 3-340-02. Supersedes TM5-1300, dated November 1990, US Department of Defense, Washington DC, 2008.
[24] Q. Dong, Q. Li, J. Zheng, Interactive mechanisms between the internal blast loading and the dynamic elastic response of spherical containment vessels, Int. J. Impact Eng. 37 (4) (2010) 349–358.
[25] V. Feldgun, Y. Karinski, I. Edri, D. Yankelevsky, Prediction of the quasi-static pressure in confined and partially confined explosions and its application to blast response simulation of flexible structures, Int. J. Impact Eng. 90 (2016) 46–60.
[26] M. Silvestrini, B. Genova, F. Leon Trujillo, Energy concentration factor. A simple concept for the prediction of blast propagation in partially confined geometries, J. Loss Prev. Process Ind. 22 (4) (2009) 449–454.
[27] S. Yao, D. Zhang, Z. Lu, Y. Lin, F. Lu, Experimental and numerical investigation on the dynamic response of steel chamber under internal blast, Eng. Struct. 168 (2018) 877–888.
[28] G. Langdon, S. Kriek, G. Nurick, Influence of venting on the response of scaled aircraft luggage containers subjected to internal blast loading, Int. J. Impact Eng. 141 (2020) 103567.
[29] C. Geretto, S. Yuen, G. Nurick, An experimental study of the effects of degrees of confinement on the response of square mild steel plates subjected to blast loading, Int. J. Impact Eng. 79 (2015) 32–44, Recent development of experimental techniques under impact loading- IUTAM Symposium, Xian, 2013.

[30] N. Jacob, G. Nurick, G. Langdon, The effect of stand-off distance on the failure of fully clamped circular mild steel plates subjected to blast loads, Eng. Struct. 29 (10) (2007) 2723–2736.
[31] Y. Yuan, C. Zhang, Y. Xu, Influence of standoff distance on the deformation of square steel plates subjected to internal blast loadings, Thin-Walled Struct. 164 (2021) 107914.
[32] B.S. Elveli, M.B. Iddberg, T. Børvik, V. Aune, On the strength-ductility trade-off in thin blast-loaded steel plates with and without initial defects - An experimental study, Thin-Walled Struct. 171 (2022) 108787.
[33] W. Noh, CEL: A time-dependent two-space-dimensional coupled Eulerian-Lagrangian code, in: B. Alder, S. Fernbach, M. Rotenberg (Eds.), Methods in Computational Physics, vol. 3, Academic Press, New York, 1964, pp. 117–179.
[34] C. Hirth, A. Amsden, J. Cook, An Arbitrary Lagrangian-Eulerian computing method for all flow speeds, J. Comput. Phys. 14 (1974) 227–253.
[35] J. Donea, P. Fasoli-Stella, P. Giuliani, Lagrangian and eulerian finite element techniques for transient fluid-structure interaction problems, in: Transactions of the 4th International Conference on Structural Mechanics in Reactor Technology, 1977.
[36] T. Belytschko, J. Kennedy, Computer models for subassembly simulation, Nucl. Eng. Des. 49 (1978) 17–38.
[37] T. Belytschko, J. Kennedy, D. Schoeberle, Quasi-Eulerian finite element formulation for fluid structure interaction, J. Press. Vessel Technol. 102 (1980) 62–69.
[38] T. Hughes, W. Liu, T. Zimmermann, Lagrangian-Eulerian finite element formulation for incompressible viscous flows, Comput. Methods Appl. Mech. Engrg. 29 (1981) 329–349.
[39] M. Souli, A. Ouahsine, L. Lewin, ALE formulation for fluid–structure interaction problems, Comput. Methods Appl. Mech. Engrg. 190 (5) (2000) 659–675.
[40] C. Zheng, X. shao Kong, W. guo Wu, S. xi Xu, Z. wei Guan, Experimental and numerical studies on the dynamic response of steel plates subjected to confined blast loading, Int. J. Impact Eng. 113 (2018) 144–160.
[41] G. Langdon, A. Ozinsky, S. Chung Kim Yuen, The response of partially confined right circular stainless steel cylinders to internal air-blast loading, Int. J. Impact Eng. 73 (2014) 1–14.
[42] T. Børvik, A. Hanssen, M. Langseth, L. Olovsson, Response of structures to planar blast loads – A finite element engineering approach, Comput. Struct. 87 (9) (2009) 507–520.
[43] L. Olovsson, Corpuscular method for airbag deployment simulations in LS-DYNA, Tech. rep., IMPETUS Afea AB, ISBN: 978-82-997587-0-3, 2007.
[44] L. Olovsson, A. Hanssen, T. Børvik, M. Langseth, A particle-based approach to close-range blast loading, Eur. J. Mech. A Solids 29 (1) (2010) 1–6.
[45] T. Børvik, L. Olovsson, A. Hanssen, K. Dharmasena, H. Hansson, H. Wadley, A discrete particle approach to simulate the combined effect of blast and sand impact loading of steel plates, J. Mech. Phys. Solids 59 (5) (2011) 940–958.
[46] M. Kristoffersen, K.O. Hauge, A. Minoretti, T. Børvik, Experimental and numerical studies of tubular concrete structures subjected to blast loading, Eng. Struct. 233 (2021) 111543.
[47] E. Fagerholt, 2008, https://www.ntnu.edu/kt/ecorr. (Online; accessed 23-May-2022).
[48] Kistler, Pressure sensor Type 603B, 2022, https://www.kistler.com/files/document/000-012e.pdf. (Online; accessed 11-November-2022).
[49] SSAB, Docol automotive steels, 2022, https://www.ssab.com/en-us/brands-and-products/docol/automotive-steel-grades/dual-phase-steel/docol-600dp. (Online; accessed 23-June-2022).
[50] G. Gruben, M. Langseth, E. Fagerholt, O. Hopperstad, Low-velocity impact on high-strength steel sheets: An experimental and numerical study, Int. J. Impact Eng. 88 (2016) 153–171.
[51] R. Kaufmann, S. Olufsen, E. Fagerholt, V. Aune, Reconstruction of surface pressures on flat plates impacted by blast waves using the virtual fields method, Int. J. Impact Eng. 171 (2023) 104369.
[52] T. Børvik, O.S. Hopperstad, T. Berstad, M. Langseth, A computational model of viscoplasticity and ductile damage for impact and penetration, Eur. J. Mech. A 20 (2001) 685–712.
[53] M.G. Cockcroft, D.J. Latham, Ductility and workability of metals, J. Inst. Metals 96 (1968) 33–39.
[54] LS-DY.N.A. Keyword User's Manual Volume I, version 13, Livermore Software Technology Corporation, Livermore, California, 2021, URL https://www.dynasupport.com/manuals/ls-dyna-manuals/ls-dyna_manual_volume_i_r13.pdf.
[55] N. Jones, Structural Impact, Cambridge University Press, 2011.